

Université de Neuchâtel

Institut de Microtechnique

**High Resolution Differential Laser
Interferometry for the VLTI
(Very Large Telescope Interferometer)**

Thèse

présentée à la Faculté des sciences
pour obtenir le grade de docteur ès sciences

par

Olivier Scherler

Neuchâtel, juin 2006

IMPRIMATUR POUR LA THESE

High resolution differential laser interferometry for the VLTI (Very Large Telescope Interferometer)

Olivier SCHERLER

UNIVERSITE DE NEUCHATEL

FACULTE DES SCIENCES

La Faculté des sciences de l'Université de Neuchâtel,
sur le rapport des membres du jury

MM. R. Dändliker (directeur de thèse),
H.P. Herzig, T. Lasser (Lausanne),
S. Lévêque (Garching bei München D)
et Y. Salvadé (Saint-Imier)

autorise l'impression de la présente thèse.

Neuchâtel, le 15 février 2007

Le doyen :
T. Ward

UNIVERSITE DE NEUCHATEL
FACULTE DES SCIENCES
Secrétariat-Décanat de la faculté
Rue Emile-Argand 11 CP 158
CH-2009 Neuchâtel

Space is big. Really big. You just won't believe how vastly hugely mindbogglingly big it is. I mean you may think it's a long way down the road to the chemist, but that's just peanuts to space.

(The Hitchhiker's Guide to the Galaxy)

Abstract

One method for locating extrasolar planets is to observe the lateral movement of a star in the sky caused by a planet in orbit around it. In order to detect this displacement, the angular position of the star has to be measured with high accuracy. This technique is called astrometry.

The Very Large Telescope Interferometer (VLTI) is operated by the European Southern Observatory and located at the Paranal Observatory in Chile. The purpose of the PRIMA instrument (Phase Referenced Imaging and Micro-arcsecond Astrometry) of the VLTI is to perform high-resolution astrometric measurements and high-resolution imaging of faint stars using white light interferometry, by combining the light collected by two telescopes. In order to allow the detection of extrasolar planets, the astrometric measurement has to be performed with micro-arcsecond accuracy.

In astrometric mode the PRIMA instrument observes two targets at the same time: the object of scientific interest, and a bright reference star. The angular position of the science object relative to the reference star is obtained by monitoring the differential optical path travelled by the light of each object in two separate white-light interferometers.

The aim of this work was to develop a high-resolution laser metrology based on superheterodyne interferometry, with an accuracy of 5 nm over a differential optical path of 100 mm. Moreover the laser source had to be stabilised on an absolute frequency reference, in order to ensure the long-term stability and calibration required to achieve the target performance. Superheterodyne interferometry allowed the direct measurement of the differential optical path using two heterodyne interferometers working with two different frequency shifts. The differential phase measurement between the two interferometers was obtained by electronic mixing of the two heterodyne signals, leading to the differential optical path needed for the astrometric measurement.

Keywords: Metrology, Interferometry, Superheterodyne Detection, Laser Stabilisation, Very Large Telescope Interferometer.

Contents

1	Introduction	1
2	The Very Large Telescope Interferometer	5
2.1	Principle of the PRIMA instrument	5
2.2	Requirements for the laser metrology	8
2.3	Concept of the PRIMA laser metrology	9
2.4	Summary of the requirements for the PRIMA metrology	14
3	Digital phasemeter for superheterodyne detection	15
3.1	Superheterodyne detection	15
3.1.1	Frequency shifter module	15
3.1.2	Electronic signal processing	17
3.2	Digital phase measurement	21
3.2.1	Phase-locked loop	21
3.2.2	Digital zero-crossing phasemeter	22
3.2.3	Averaging of phase data	27
3.2.4	Error compensation fringe counter	28
3.2.5	Status registers	29
3.2.6	Data transfer	30

4	Frequency stabilisation of a Nd:YAG laser	31
4.1	Frequency noise of the laser	31
4.1.1	Measurement of the beat frequency	31
4.1.2	Measurements at large OPD	32
4.1.3	Required frequency noise spectrum	35
4.2	Absolute stabilisation	36
4.2.1	Absolute frequency references	36
4.2.2	Stabilisation of the second-harmonic wavelength on iodine	37
4.2.3	Centre-of-fringe locking	37
4.3	Second-harmonic generation	40
4.3.1	Birefringent phase matching	40
4.3.2	Conversion efficiency	41
4.3.3	Birefringent walk-off	45
4.3.4	Quasi-phase matching in periodically-poled crystals	47
4.4	Set-up for the laser stabilisation	48
4.4.1	Second harmonic generation	49
4.4.2	Frequency modulation	49
4.4.3	Absorption	50
4.4.4	Optical detection	50
4.4.5	Control loop	51
5	Tests of the phasemeter and of the laser stabilisation	53
5.1	Tests of the phasemeter	53
5.1.1	Electrical tests of the phasemeter	53
5.1.2	Test of accuracy using two-wavelength interferometry	57
5.1.3	Dynamic tests	59
5.2	Tests of the laser stabilisation	64
5.2.1	Characterisation of the iodine cell	64

5.2.2	Error signal monitoring	67
5.2.3	Test with long delay lines	68
5.2.4	Further tests performed at ESO	69
6	Conclusion	73
	Acknowledgements	77
	Bibliography	79

Chapter 1

Introduction

The Very Large Telescope Interferometer (VLTI), operated by the European Southern Observatory and located at the Paranal Observatory in Chile, generates interference fringes by combining the light collected by two telescopes observing a single object. The PRIMA instrument of the VLTI [1, 2] aims to perform high-resolution astrometric measurements and phase-referenced imaging by observing the interference fringes of two objects at the same time and by monitoring the optical path travelled by the light in these two interferometers. The objective of this instrument is the detection of extra-solar planets as well as high-resolution imaging of faint stars.

For these measurements, the knowledge of the differential optical path between the two stellar interferometers is needed. Superheterodyne detection was therefore proposed for this purpose.

Superheterodyne detection was developed for two-wavelength interferometry by Dändliker et al. [3]. In two-wavelength interferometry, a synthetic wavelength Λ is generated from two individual wavelengths λ_1 and λ_2 and can be chosen to be much longer than the optical wavelengths. Measurement of the phase at the synthetic wavelength allows one to reduce the sensitivity or to extend the range of unambiguity for interferometric measurements.

Superheterodyne detection uses two different heterodyne frequencies f_1 and f_2 for the individual wavelengths λ_1 and λ_2 to permit high-resolution phase measurements at the synthetic wavelength without optical separation of the individual wavelengths. By feeding the two heterodyne signals to an electronic mixer, it is possible to measure the phase

difference directly. For the VLTI, superheterodyne detection is not used to measure a single optical path with two different wavelengths (as originally intended), but to measure two distinct optical paths with a single wavelength.

The present work is the result of a collaboration between IMT (Institute of Microtechnology, Neuchâtel) and ESO (European Southern Observatory, Garching bei München). It was supported by the FINES program of the Swiss National Science Foundation.

The goal of this work was to develop a high-resolution laser metrology based on superheterodyne interferometry, capable of measuring the differential optical path between two distinct interferometers with 5 nm accuracy, without having to take two separate phase measurements and compute their difference. Moreover, the laser source had to be stabilised on an absolute frequency reference in order to ensure the long-term stability and calibration required to achieve the target resolution of 1 nm over 100 mm.

Part of this work has already been published or presented at international conferences:

- [A] S. Lévêque, Y. Salvadé, O. Scherler and R. Dändliker, “High accuracy laser metrology enhances the VLTI,” *Laser Focus World* **38** (4), 101–104 (2002).
- [B] S. A. Lévêque, R. Wilhelm, Y. Salvadé, O. Scherler and R. Dändliker, “Toward nanometer accuracy laser metrology for phase-referenced interferometry with the VLTI,” in W. A. Traub, ed., “Interferometry for Optical Astronomy II,” vol. 4838, pp. 983–994, SPIE (2003)

The principle of the PRIMA instrument of the VLTI is described in **chapter 2**. The need for a high-accuracy laser metrology is explained and the specifications are derived from the expected performance of PRIMA. The underlying concepts of heterodyne and superheterodyne interferometry are then presented.

Chapter 3 describes the optics and analogue electronics that were designed to implement superheterodyne detection, as well as the digital electronics that were built to perform the phase measurement. Emphasis has been put on the critical points that had to be addressed in order to meet the specifications.

The frequency stabilisation of the metrology laser is presented in **chapter 4**. First, the measurements of the frequency noise of the laser are discussed. The concept that was selected for the stabilisation is then explained, including a discussion pertaining to the generation of the second harmonic of the laser. Finally, the stabilisation set-up is described.

Chapter 5 summarises all the tests that were performed on the digital phasemeter and on the stabilised laser in order to verify their performance. Finally, in-situ modifications and tests of the stability of the laser are presented.

Chapter 2

The Very Large Telescope Interferometer

2.1 Principle of the PRIMA instrument

The Very Large Telescope (VLT), located at the Paranal Observatory in Chile comprises four fixed unit telescopes (UT) of 8.2 m diameter and four movable auxiliary telescopes (AT) of 1.8 m diameter that can be positioned over thirty different stations. The VLT operating in interferometric mode is called the Very Large Telescope Interferometer (VLTI). In this mode, two telescopes are used at the same time to form a stellar interferometer.

The VLTI generates interference fringes from a stellar object by combining the light collected by two telescopes distant by several meters. Since the object is a wide spectrum source, delay lines operating between the telescopes and the interferometric laboratory are used to equal the optical paths followed by the stellar light through each telescope, making the interference possible. Observation of the interference fringes then allows the reconstruction of an image of the object with an increased resolution compared to that of a single telescope.

The PRIMA instrument (Phase Referenced Imaging and Micro-arcsecond Astrometry) aims to improve the performance of the VLTI by observing at the same time as the object of interest (science object) a bright reference star close to it [1]. The light from

both objects travels through a delay line which is controlled by observing the interference fringes of the reference star and ensures the compensation of the optical path between the two telescopes. A differential delay line is then used to apply the necessary remaining compensation to the path followed by the light of the science object.

By measuring the optical path travelled by the light of each object using a high-accuracy metrology, the differential compensation applied between them can be measured. The knowledge of this quantity allows to improve the performance of the VLTI in several ways:

- Longer integration times are possible, giving access to fainter objects;
- The resolution of the image reconstruction can be increased by phase referenced imaging;
- High resolution astrometric measurements up to $10 \mu\text{arcsec}$ can be performed.

Layout of the VLTI

Figure 2.1 shows the layout of the VLT during interferometric operation. The light from the stellar object is collected using two telescopes and the white light interferometry fringes are observed on the fringe sensor unit (FSU). In order for fringes to be present, the optical path in both arms of the interferometer must be equal. This is achieved by means of moving delay lines between the telescopes and the fringe sensor unit.

The PRIMA instrument consists of two stellar interferometers, one for the reference star and one for the science object. The main delay line affects the path of both interferometers in the same way. It is controlled by tracking the interference fringes of the reference star and applies the corrections needed to compensate the effects of the rotation of Earth and of the atmospheric fluctuations on the optical paths. The differential delay line only affects the optical path of the science interferometer and is controlled by tracking the fringes of the science object on a second FSU.

In astrometric mode, the PRIMA metrology measures the distance compensation applied to the reference and science interferometers L_1 and L_2 , respectively, by means of a laser interferometer in common path with the stellar light. As shown on Fig. 2.2, L_1 and L_2 depend on the distance between the telescopes, which is called the baseline (B), and the angular position of the corresponding object. By measuring the differential compensation $\Delta L = L_1 - L_2$, it is possible to calculate the angular separation between the reference and science objects.

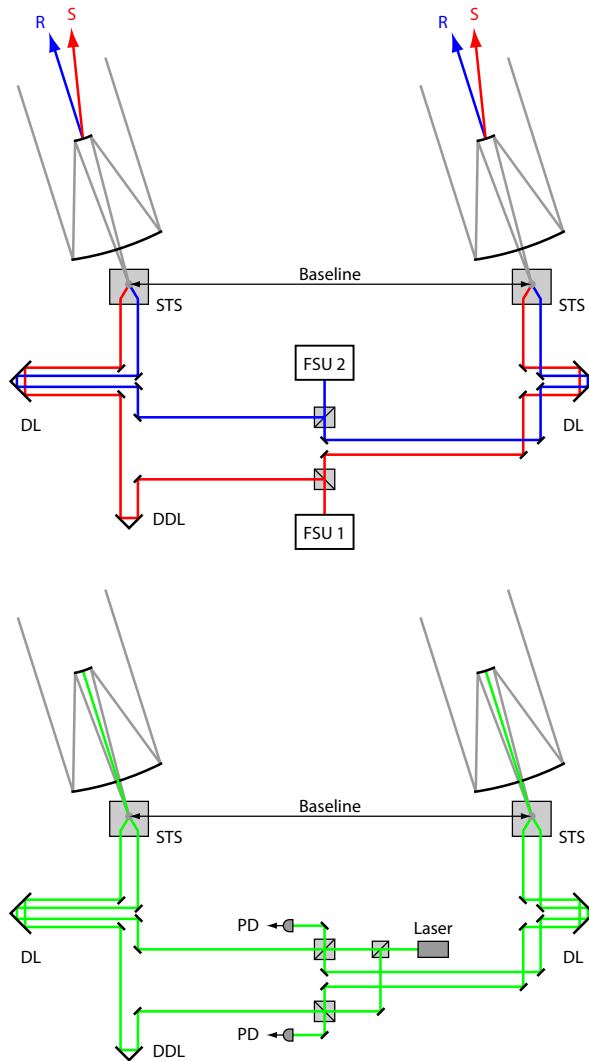


Figure 2.1: Schematic of the VLTI. Top: the main delay line (DL) tracks the interference fringes of the reference star (R) on the first fringe sensor unit (FSU 1) in order to compensate the effects of the rotation of Earth and of the atmospheric fluctuations. The differential delay line (DDL) tracks the fringes of the science object (S) on the second FSU. Bottom: The laser metrology measures the differential optical path ΔL . STS: Star separator, PD: Metrology photodetector.

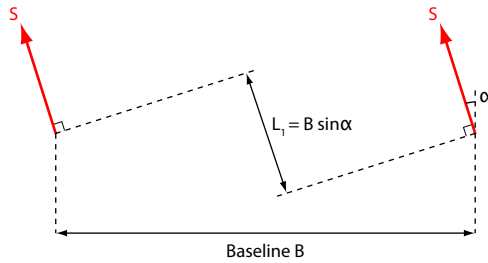


Figure 2.2: Dependence of the distance compensation (L_1) on the baseline (B) and the angular position of the object (α).

2.2 Requirements for the laser metrology

The target accuracy for PRIMA in astrometric mode is of $10 \mu\text{arcsec}$, or 5×10^{-11} rad, with a baseline of 100 m. This leads to a requirement on the accuracy of the measurement of ΔL of 5 nm, with a target resolution of less than 1 nm. This resolution must be reached with a minimum optical power of 20 nW. With a baseline of 200 m, the maximum star separation of 1 arcmin leads to a maximum ΔL of 60 mm. Therefore, a target range for the metrology system of 100 mm was specified.

The maximum velocity of the main delay lines (DL) and of the differential delay line (DDL) at which the PRIMA metrology system should operate with the specified accuracy is 10 mm/s for the DL and 15 mm/s for the DDL. The maximum velocity for which the system should be able to keep track of the interference fringes (slewing velocity) is 36 mm/s for the DL and 18 mm/s for the DDL.

The rate of the data delivered by the metrology system should be selectable between 0.5 Hz and 8 kHz, with the value of ΔL averaged over the measurement period.

The laser source should have a wavelength above $1 \mu\text{m}$ to avoid stray light on the Silicon photodetectors used for the adaptive optics of the VLT, but below $2 \mu\text{m}$ where astronomical observations are performed. The coherence length should be larger than 500 m. Therefore, a Nd:YAG laser at 1319 nm was chosen. In order to reach the target resolution of 1 nm over a range of 100 mm, the optical frequency of the laser should be stable to 10^{-8} and known with the same accuracy. The requirements are summarised in Table 2.1.

Differential OPD (ΔL)	Resolution	< 1 nm
	Accuracy	< 5 nm
	Max. range	100 mm
	Min. optical power	20 nW
Max. operating velocity	DL	10 mm/s
	DDL	15 mm/s
Max. slewing velocity	DL	36 mm/s
	DDL	18 mm/s
Output	Data rate	0.5 Hz – 8 kHz
Laser source	Wavelength	1319 nm
	Frequency stability	10^{-8}

Table 2.1: Summary of the requirements for the PRIMA laser metrology.

2.3 Concept of the PRIMA laser metrology

The value measured by the PRIMA metrology is $\Delta L = L_1 - L_2$, the difference between the optical path differences (OPD) of the reference and the science interferometers (Fig. 2.3). We call L_{11} and L_{12} the arm lengths of the science interferometer and $L_1 = L_{12} - L_{11}$ the OPD of the interferometer. Similarly, the arm lengths and the OPD of the reference interferometers are called L_{21} , L_{22} and $L_2 = L_{22} - L_{21}$, respectively. Two laser interferometers are used to measure L_1 and L_2 from the interferometric phases ϕ_1 and ϕ_2 given by

$$\phi_1 = \frac{4\pi\nu_1}{c} L_1, \quad \phi_2 = \frac{4\pi\nu_2}{c} L_2. \quad (2.1)$$

A solution to measure ΔL is to measure ϕ_1 and ϕ_2 separately and compute the differential OPD using the relation

$$\Delta L = \frac{c}{4\pi\nu_1} \phi_1 - \frac{c}{4\pi\nu_2} \phi_2. \quad (2.2)$$

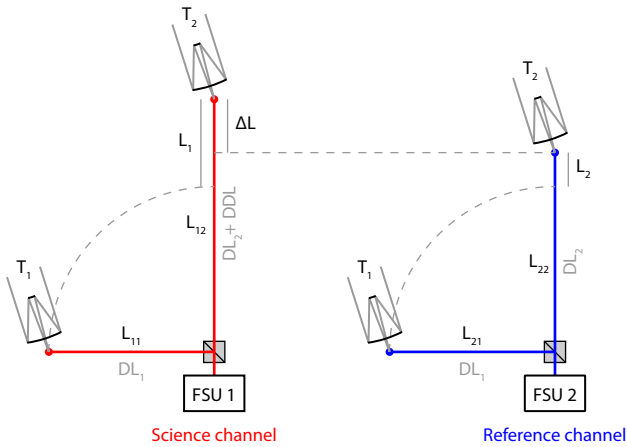


Figure 2.3: Concept of the PRIMA laser metrology. T: telescopes, DL: delay lines, DDL: differential delay line, FSU: fringe sensor units.

However, the two independent measuring systems should be able to monitor the individual phases at the maximum frequency of the fluctuations, which is given by the maximal tracking speed of the delay line and is about 25 kHz. Moreover, in order to reach the required accuracy of 5 nm with delay lines moving at 15 mm/s, the two measurements must be not be separated by more than

$$\Delta t = \frac{5 \text{ nm}}{2 \cdot 15 \text{ mm/s}} = 0.17 \mu\text{s}. \quad (2.3)$$

On the other hand, if the phase difference could be measured directly, there would be no simultaneity issues and since the differential OPD varies much slower than the individual paths, the measurement could be performed with a longer integration time by averaging over many cycles. To achieve this, a technique called superheterodyne interferometry is used.

Heterodyne interferometry

In classical, homodyne interferometry, the interference signal $I(L)$ is of the form

$$I(L) = |U_1|^2 + |U_2|^2 + 2|U_1||U_2|\cos(\Delta\phi), \quad (2.4)$$

with

$$\Delta\phi = \frac{4\pi\nu}{c} L, \quad (2.5)$$

where $\Delta\phi$ is the phase difference of the interferometer, L the optical path difference and U_1 and U_2 are the amplitudes of the waves in each arm.

In heterodyne interferometry, however, a small shift f of the optical frequency of a few tens of MHz is introduced between the two arms of the interferometer. The complex amplitudes of the two interfering waves are therefore given by

$$\begin{aligned} U_1(z, t) &= U_{01} e^{i\phi_1} e^{i2\pi\nu t}, \\ U_2(z, t) &= U_{02} e^{i\phi_2} e^{i2\pi(\nu+f)t}, \end{aligned} \quad (2.6)$$

and the interference signal becomes

$$\begin{aligned} I(t) &= |U_{01}|^2 + |U_{02}|^2 + 2|U_{01}||U_{02}|\cos(2\pi ft + \Delta\phi) \\ &= I_1 + I_2 + 2\sqrt{I_1 I_2} \cos(2\pi ft + \Delta\phi). \end{aligned} \quad (2.7)$$

Superheterodyne interferometry

In order to measure ΔL directly, without having to measure L_1 and L_2 separately and compute the difference, a technique called superheterodyne interferometry is used [3]. It consists of using two different heterodyne frequencies, f_1 and f_2 , in the two interferometers. Moreover, in order to avoid any crosstalk, an additional frequency offset f_0 is introduced between the two interferometers. Therefore, the optical frequencies are ν and $\nu + f_1$ for the science interferometer and $\nu + f_0$ and $\nu + f_0 + f_1$ for the reference interferometer.

The interference signal for the two interferometers can be written as

$$\begin{aligned} I_1(t) &= I_{11} + I_{12} + 2\sqrt{I_{11}I_{12}}\cos(2\pi f_1 t + \phi_1), \\ I_2(t) &= I_{21} + I_{22} + 2\sqrt{I_{21}I_{22}}\cos(2\pi f_2 t + \phi_2), \end{aligned} \quad (2.8)$$

where I_{11} and I_{12} are the intensities in each arm of the science interferometer, ϕ_1 is the phase difference of the science interferometer, and likewise I_{21} , I_{22} and ϕ_2 for the reference interferometer.

The phase difference of the science interferometer is linked to the OPD by

$$\phi_1 = \frac{4\pi(\nu + f_1)}{c} L_{12} - \frac{4\pi\nu}{c} L_{11} = \frac{4\pi\nu}{c} L_1 + \frac{4\pi f_1}{c} L_{12}. \quad (2.9)$$

Since only one delay line, L_{11} , is moving the other one being passive, the term containing L_{12} will be constant. The phase therefore only varies with L_1

$$\phi_1 = \frac{4\pi\nu}{c} L_1. \quad (2.10)$$

Similarly, the phase of the reference interferometer depends on L_2 by

$$\phi_2 = \frac{4\pi(\nu + f_0)}{c} L_2. \quad (2.11)$$

Superheterodyne detection consists of mixing both interference signals electronically after detection. The signals are bandpass filtered around their heterodyne frequencies in order to keep only the ac part, then they are mixed together and the result is bandpass filtered around the difference between the two heterodyne frequencies. The result of mixing the signals is their multiplication, which yields

$$\begin{aligned} I(t) &\propto \sqrt{I_{11}I_{12}} \cos(2\pi f_1 t + \phi_1) \cdot \sqrt{I_{21}I_{22}} \cos(2\pi f_2 t + \phi_2) \\ &= I_0 \left[\cos(2\pi(f_1 + f_2)t + \phi_1 + \phi_2) \right. \\ &\quad \left. + \cos(2\pi(f_1 - f_2)t + \phi_1 - \phi_2) \right]. \end{aligned} \quad (2.12)$$

Filtering around $f_1 - f_2$ gives

$$I(t) = I_0 \cos(2\pi(f_1 - f_2)t + \phi_1 - \phi_2). \quad (2.13)$$

In order to measure the phase $\phi_1 - \phi_2$ that leads to ΔL , a reference signal of the same frequency with fixed phase must be generated. The superheterodyne detection process is depicted on Fig. 2.4. From Eqs. (2.10) and (2.11), we get for the phase difference

$$\begin{aligned} \phi_1 - \phi_2 &= \frac{4\pi\nu}{c} L_1 - \frac{4\pi(\nu + f_0)}{c} L_2 \\ &= \frac{4\pi\nu}{c} \Delta L - \frac{4\pi f_0}{c} L_2. \end{aligned} \quad (2.14)$$

We can see that due to the frequency offset f_0 between the science and reference interferometers, the measured phase not only depends on the differential OPD ΔL but also on the OPD of the reference interferometer L_2 . Therefore, the variation of this OPD must be monitored in order to be compensated. The phase shift $\delta\phi$ introduced by the variation δL_2 of the OPD is given by

$$\delta\phi = \frac{4\pi f_0}{c} \delta L_2. \quad (2.15)$$

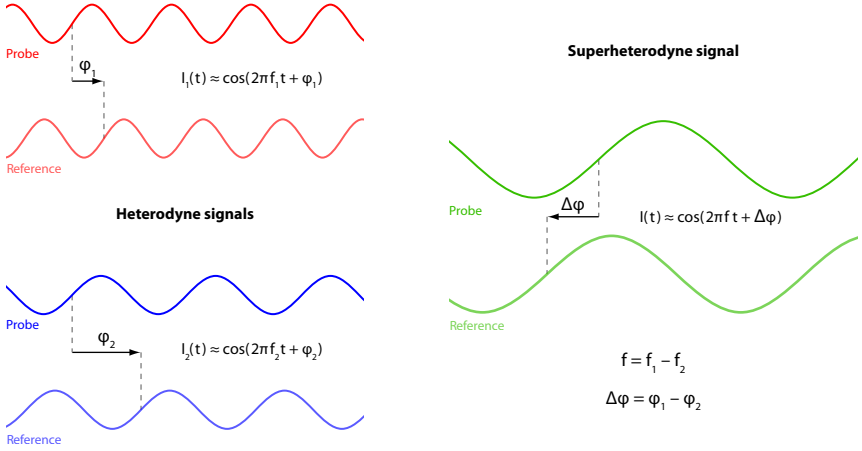


Figure 2.4: Superheterodyne detection. The electronic mixing of the two heterodyne signals $I_1(t)$ and $I_2(t)$ results in the superheterodyne signal $I(t)$, whose frequency and phase f and $\Delta\phi$ are equal to the difference of the frequencies and phases f_1 , f_2 and ϕ_1 , ϕ_2 of the heterodyne signals.

Since $\delta\phi$ depends only on the frequency difference f_0 , which is 78 MHz in our case (see Tab. 3.1), the required accuracy on δL_2 in order to achieve $2\pi/1000$ accuracy is not very stringent:

$$\Delta(\delta L_2) = \frac{c}{4\pi f_0} \frac{2\pi}{1000} = 1.9 \text{ mm.} \quad (2.16)$$

A simple fringe counter on the reference interferometer can therefore be used to monitor δL_2 within the target accuracy. If N_{FC} is the current value of the fringe counter, δL_2 is given by

$$\delta L_2 = \frac{c}{4\pi(\nu + f_0)} 2\pi N_{\text{FC}} \approx \frac{c}{2\nu} N_{\text{FC}}, \quad (2.17)$$

and

$$\delta\phi = \frac{4\pi f_0}{c} \delta L_2 = \frac{2\pi f_0}{\nu} N_{\text{FC}}. \quad (2.18)$$

Therefore, the differential OPD ΔL is given by

$$\Delta L = \frac{c}{4\pi\nu} (\phi + \delta\phi) = \frac{c}{4\pi\nu} \left(\phi + \frac{2\pi f_0}{\nu} N_{\text{FC}} \right). \quad (2.19)$$

2.4 Summary of the requirements for the PRIMA metrology

The PRIMA metrology should measure ΔL with a resolution of 1 nm ($2\pi/660$ in phase for $\lambda = 1319$ nm) and an accuracy of 5 nm ($2\pi/130$), with a maximum range of 100 mm. The minimum optical power is of 20 nW. The maximum velocities of the delay lines and of the differential delay line under operating conditions are 10 mm/s and 15 mm/s, respectively. The maximum slewing velocities of the delay lines and of the differential delay line are 36 mm/s and 18 mm/s, respectively.

The output data rate should be selectable between 0.5 Hz and 8 kHz and the internal sampling frequency (and thus the superheterodyne frequency) should be high enough to allow the averaging of the value of ΔL over several cycles.

Furthermore, the frequency of the 1319 nm Nd:YAG laser should be stable to 10^{-8} and known with the same accuracy.

Chapter 3

Digital phasemeter for superheterodyne detection

3.1 Superheterodyne detection

Figure 3.1 describes the principle of the superheterodyne phase measurement. The heterodyne signals at frequencies f_1 and f_2 are detected by four photodetectors and the superheterodyne module performs the filtering and mixing operations described in chapter 2.3. It generates the superheterodyne signals at frequency $f = f_1 - f_2$ which are then fed to the digital phasemeter that measures their phase difference $\Delta\phi$.

3.1.1 Frequency shifter module

The frequency shifter module generates the frequency shifts necessary to produce the different heterodyne signals. The goal is to generate two heterodyne signals with a frequency difference $\Delta f = f_1 - f_2$ of a few hundreds of kilohertz in order to be fast enough to allow an output averaged over several samples at the required 8 kHz, but slow enough not to introduce too stringent requirements on the analogue electronics. Moreover, there should be an offset f_0 between the optical frequencies of the two interferometers, which can be sufficiently filtered to avoid crosstalk.

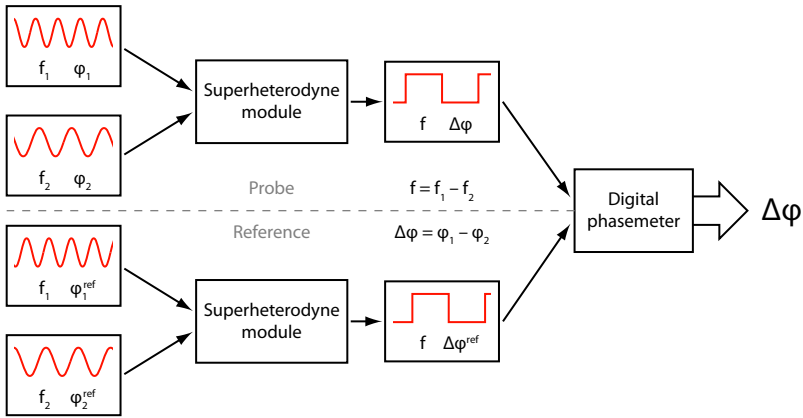


Figure 3.1: Block diagram of the PRIMA phasemeter.

We used four fibre-pigtailed acousto-optic modulators (AOM) working at frequencies near 40 MHz. In order to introduce the frequency shift $f_0 = 78$ MHz between the two interferometers, we used the first negative order of diffraction for two modulators (-38 and -38.65 MHz, $f_1 = 650$ kHz) and the first positive order for the other two ($+40$ and $+39.55$ MHz, $f_2 = 450$ kHz). Table 3.1 summarises the frequencies used and Fig. 3.2 shows the layout of the frequency shifter module.

AOM 1	AOM 2	AOM 3	AOM 4
-38 MHz	-38.65 MHz	$+40$ MHz	$+39.55$ MHz
$f_1 = 650$ kHz		$f_2 = 450$ kHz	
$\Delta f = 200$ kHz			
$f_0 = 78$ MHz			

Table 3.1: Frequency shifts and heterodyne frequencies generated by the acousto-optic modulators.

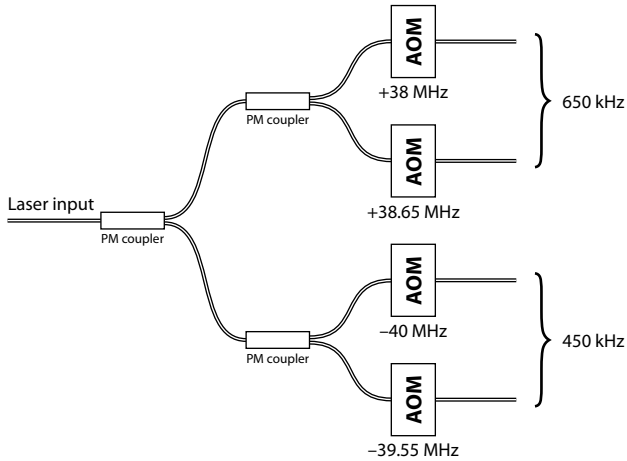


Figure 3.2: Layout of the frequency shifter module. AOM: acousto-optic modulators, PM coupler: polarisation-maintaining fibre couplers.

3.1.2 Electronic signal processing

Figure 3.3 shows the schematic of the superheterodyne module, including the photodetectors, the input bandpass filters, the mixer stage and the output bandpass filter with a limiting amplifier.

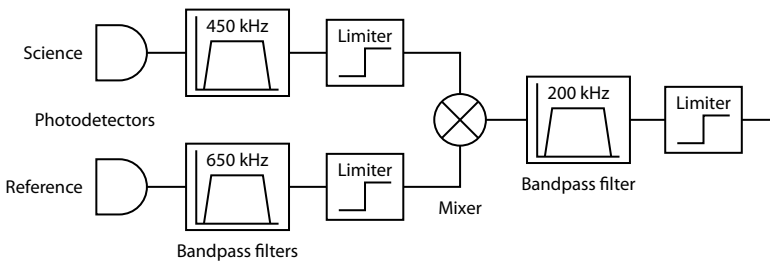


Figure 3.3: Schematic of the superheterodyne module.

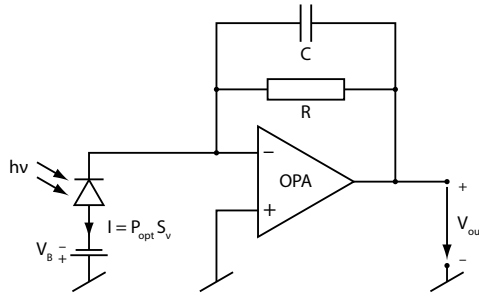


Figure 3.4: Typical photodetector circuit. PD: photodiode, OPA: operational amplifier, R: transimpedance gain.

Photodetectors

Figure 3.4 shows a typical photodetector consisting of a photodiode and a transimpedance circuit. The gain of the amplifier is given by the transimpedance resistor R . For a given optical frequency ν , the sensitivity S of the photodetector is determined by the spectral sensitivity of the photodiode S_ν and the transimpedance gain R as

$$S = R S_\nu = R \frac{\eta e}{h\nu}, \tag{3.1}$$

where η is the quantum efficiency of the photodiode and e the electron charge. The spectral sensitivity S_ν relates the current I at the output of the photodiode to the optical power P_{opt} , whereas the sensitivity of the photodetector S links the voltage V_{out} at the output of the amplifier to the optical power:

$$I = P_{opt} S_\nu, \tag{3.2}$$

$$V_{out} = RI = P_{opt} S. \tag{3.3}$$

The photodetectors of the phasemeter use InGaAs photodiodes with a spectral sensitivity of $S_\nu = 0.88 \text{ A/W}$ at $1.3 \mu\text{m}$. The transimpedance gain is $R = 1.4 \times 10^6 \text{ V/A}$, leading to a sensitivity of $S = 1.23 \text{ V}/\mu\text{W}$.

Trigger error

In a zero-crossing phasemeter, the noise on the signal introduces an uncertainty on the time of the crossing. Figure 3.5 illustrates this phenomenon. This uncertainty Δt can

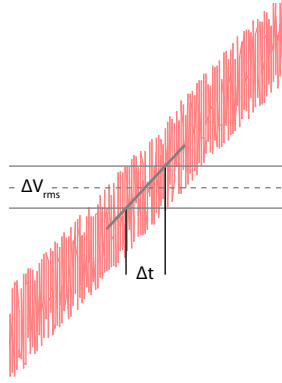


Figure 3.5: Trigger error.

be calculated from the slope of the signal and the rms noise as

$$\Delta t = \frac{\Delta V_{\text{rms}}}{\left. \frac{dV}{dt} \right|_{V=0}}. \quad (3.4)$$

In the case of a cosine signal

$$V(t) = V \cos(2\pi ft + \phi), \quad (3.5)$$

of amplitude V and frequency f , the slope is

$$\left. \frac{dV}{dt} \right|_{V=0} = 2\pi fV. \quad (3.6)$$

Assuming that both the reference and the measurement signals contribute equally to the phase error $\delta\phi$, we get

$$\delta\phi = 2\pi f \sqrt{\Delta t_{\text{meas}}^2 + \Delta t_{\text{ref}}^2} = \sqrt{2} \frac{\Delta V_{\text{rms}}}{V}. \quad (3.7)$$

The SNR, defined as the ratio of the electrical power of the signal and the electrical power of the noise, is related to the rms noise by

$$\text{SNR} = \frac{P_{\text{signal}}^{\text{el.}}}{P_{\text{noise}}^{\text{el.}}} = \frac{V^2 \langle \cos^2(2\pi ft + \phi) \rangle}{\Delta V_{\text{rms}}^2} = \frac{1}{2} \frac{V^2}{\Delta V_{\text{rms}}^2}. \quad (3.8)$$

Therefore, the phase error can be expressed in terms of the SNR as

$$\delta\phi = \frac{1}{\sqrt{\text{SNR}}}. \quad (3.9)$$

To get the required phase resolution of $2\pi/660$, the SNR of the electronic signals must be at least 11000 or, in logarithmic units, $\text{SNR} > 40$ dB.

Due to the movement of the delay lines at velocities up to 36 mm/s, the frequency of the heterodyne signals is shifted by the Doppler effect during operation. In order to avoid introducing a phase shift that depends on the movement of the delay lines, the phase response of the photodetectors should be as flat as possible. In this intent, the bandwidth of the transimpedance amplifier was designed to be 7.5 MHz, which is much higher than the frequency of the detected signals.

Bandpass filters

Tenth order Chebyshev bandpass filters are used to extract the heterodyne frequencies. However, the Doppler shift caused by the movement of the delay lines changes the frequencies and if the phase responses of the 450 kHz and 650 kHz filters are different, a phase shift dependent on the velocity of the delay lines will be introduced. Therefore, the phase response of the filters have to be matched to within $2\pi/660$ (0.54 deg) over a width of 110 kHz, corresponding to the range of Doppler frequencies caused by the maximum speed of the delay lines of 36 mm/s. It is not trivial to fulfil this requirement because the two bandpass filters operate around two different frequencies.

Limiting amplifiers and mixer

The 450 kHz and 650 kHz heterodyne signals are mixed and filtered around the superheterodyne frequency $f = 200$ kHz. The filters have a bandwidth of 55 kHz, corresponding to the maximum Doppler shift caused by the movement of the differential delay line at a velocity of 18 mm/s.

During the testing of the prototype version of the phasemeter, it was noticed that variations of the amplitude of the heterodyne signals at the input of the mixer caused variations of the phase of the superheterodyne signal. To solve this problem, limiting amplifiers were introduced at the mixer inputs to convert the sinusoidal heterodyne signals into square signals of constant amplitude. Other benefits of this configuration are that the mixing efficiency is higher compared to sinusoidal signals and that the amplitude

of the square signals can be adjusted for maximum efficiency using an amplifier with a variable gain at the input of the mixer. Another limiting amplifier was placed after the output bandpass filter of the mixer to convert the superheterodyne signal into a square signal fed to the digital phasemeter.

The limiting amplifiers are composed of two stages. The first stage amplifies the signal with a high gain and limits the amplitude using diodes and the second stage is a comparator that delivers a square signal in TTL format. The high gain of the amplifier results in an increased slope of the signal at zero-crossing, which renders the system less sensitive to an offset of the comparator.

3.2 Digital phase measurement

The purpose of the digital phasemeter is to measure the phase between the 200 kHz reference and probe superheterodyne signals with a resolution of at least $2\pi/660$. It should be able to monitor displacements of the differential delay line up to 120 mm and should perform averaging of data in order to measure with a frequency response between 0.5 Hz and 8 kHz.

Moreover, due to the frequency offset f_0 between the science and reference channels, the OPD of the reference interferometer L_2 has to be monitored using a fringe counter on the 450 kHz heterodyne signal, as explained in chapter 2.3.

The digital logic of the phasemeter was implemented using programmable logic devices (PLD) of the MAX7000 family from Altera.

3.2.1 Phase-locked loop

A phase-locked loop (PLL) was used to generate the clock signals necessary to the operation of the digital phasemeter. A 200 MHz primary clock drives the fractional phase-meter and a 50 MHz clock is used for the rest of the circuit, which can operate at lower speed.

Figure 3.6 shows the principle of the PLL. It is composed of a high-frequency voltage-controlled oscillator (VCO) at 200 MHz and of a phase comparator circuit. The VCO frequency is divided by 1024 to obtain a signal of roughly 200 kHz. The phase of this signal is then compared to the phase of the reference superheterodyne signal. The low-pass filtered output of the phase comparator is fed back to the VCO. When the PLL

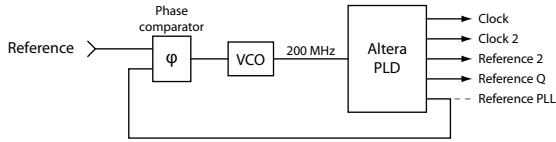


Figure 3.6: Schematic of the phase-locked loop. Reference: reference superheterodyne signal at 200 kHz, Clock: 200 MHz primary clock, Clock 2: 50 MHz secondary clock, Reference 2: reference signal after clock synchronisation, Reference Q: reference signal in quadrature, Reference PLL: VCO frequency divided by 1024.

is locked, the frequency at the output of the VCO is 1024 times the frequency of the reference signal, or 200 MHz.

We used a Mini-Circuits POS-400P VCO and the phase comparator of an HEF4046BF PLL circuit. The frequency division was implemented with a digital counter in an Altera PLD. Moreover, the same device was used to generate the secondary clock signal at 50 MHz as well as a reference signal in quadrature (phase shifted by $\pi/2$) used by the fractional phasemeter. Both the reference and the reference in quadrature were also synchronised with the primary clock to avoid stability problems in the digital phasemeter due to asynchronous signals.

3.2.2 Digital zero-crossing phasemeter

Fractional phase

Figure 3.7 shows the principle of operation of a digital phasemeter. The goal is to measure the phase between a reference and a probe signal of the same known frequency f . This is achieved by measuring the time between a raising edge of the reference signal and a raising edge of the probe signal, using a digital counter. The counter is driven with a clock signal whose frequency f_c gives the resolution $\delta\phi$ of the phasemeter. The phase ϕ is calculated from the value of the counter N_ϕ and the resolution $\delta\phi$. N_ϕ ranges from 0 to N_1 , corresponding to phases between 0 and 2π . Since the frequency multiplier of the phase-locked loop must be a power of two and the resolution of the phasemeter must be at least $2\pi/660$, the best value for N_1 is 1024 and the counter has 10 bits.

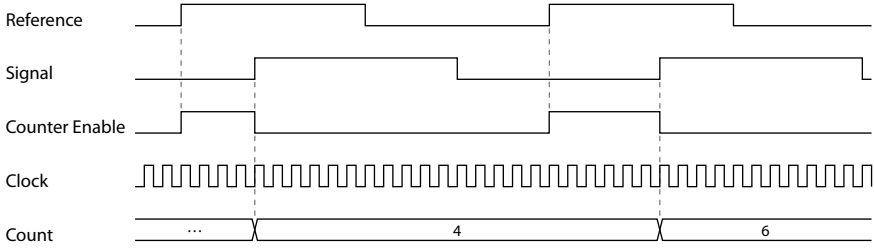


Figure 3.7: Principle of operation of a digital phasemeter. In this example the clock frequency is 20 times higher than the signal frequency, therefore the resolution is $2\pi/20$. After the first measurement, the value of the counter is 4, corresponding to a phase of $2\pi/5$ or 72 deg.

The clock frequency f_c is the frequency of the superheterodyne signal f multiplied by the PLL multiplier N_1 :

$$f_c = N_1 f. \quad (3.10)$$

With a heterodyne signal at $f = 200$ kHz, the clock frequency of the digital phasemeter is thus 204.8 MHz.

For the phase resolution $\delta\phi$, which is given by the ratio of the signal and clock frequencies, we get then

$$\delta\phi = 2\pi \frac{f}{f_c} = \frac{2\pi}{N_1} = \frac{2\pi}{1024}, \quad (3.11)$$

and the phase ϕ for a given measurement is calculated from the resolution and the value of the counter N_ϕ by

$$\phi = N_\phi \delta\phi = 2\pi \frac{N_\phi}{N_1}. \quad (3.12)$$

In practice, problems can occur when the phase is near zero, because if the edges of the reference and probe signals are too close to each other, a new measurement could start before the previous one is read-out, resulting in an output value of zero. The solution is to use a second counter driven by a reference signal in quadrature to the other, i.e. phase shifted by $\pi/2$. This way, for any phase, at least one of the two counters is read-out at the appropriate time and provides a valid phase value. When the value of the main

counter is zero, the value of the quadrature counter is used instead, after being corrected to compensate for the phase shift introduced by the reference signal in quadrature.

Since the reference signal in quadrature is delayed by $\pi/2$, the correction that should be added to the value of the counter is $N_1/4 = 256$. Since N_1 is a power of two, this operation can be easily achieved by acting only on the two most significant bits of N_ϕ . Equation (3.13) illustrate the logical operations used to perform this addition,

$$\begin{array}{rcccc}
 & & F_{n-2} & & \\
 & & F_{n-1} & F_{n-2} & \dots & F_0 \\
 + & & 0 & 1 & \dots & 0 \\
 \hline
 & F_{n-2} \oplus F_{n-1} & \bar{F}_{n-2} & \dots & F_0 &
 \end{array} \tag{3.13}$$

where $n = 10$ is the maximum bit number of the counter and F_{n-1} and F_{n-2} are the two most significant bits of the fractional phase measured by the quadrature counter.

Integer phase

In addition to the fractional phasemeter, an integer fringe counter is needed in order to keep track of the distance covered by the delay lines. An up/down counter is triggered every time the fractional phase crosses zero, with the direction of the count matching the direction of the crossing.

Figure 3.8 shows the control signals used to enable the counter and to choose the direction. The range of values of the fractional phase is split into four quadrants. The counter is triggered by the clock signal CCK every time the phase changes quadrants. If the previous and current values of Cnt are 1, it means that the value crossed zero and the counter is enabled. The counting direction is given by the UD signal. Equations (3.14)–(3.16) show how the control signals are generated from the two MSBs of the fractional phase

$$\text{Cnt} = \overline{\bar{F}_{n-2}^{\text{prev}} \oplus \bar{F}_{n-2}} \tag{3.14}$$

$$\text{UD} = \overline{F_{n-1} \oplus F_{n-2}} \tag{3.15}$$

$$\text{CCK} = \text{UD}^{\text{prev}} \oplus \text{UD} \tag{3.16}$$

Figure 3.9 shows the logic diagram of the fractional phasemeter. Counter A is enabled on an edge of the reference signal, whereas counter B is enabled on an edge of the reference signal in quadrature. On the next edge of the probe signal, both counters are disabled, their values are loaded in a buffer and the counters are reset. The value of the quadrature

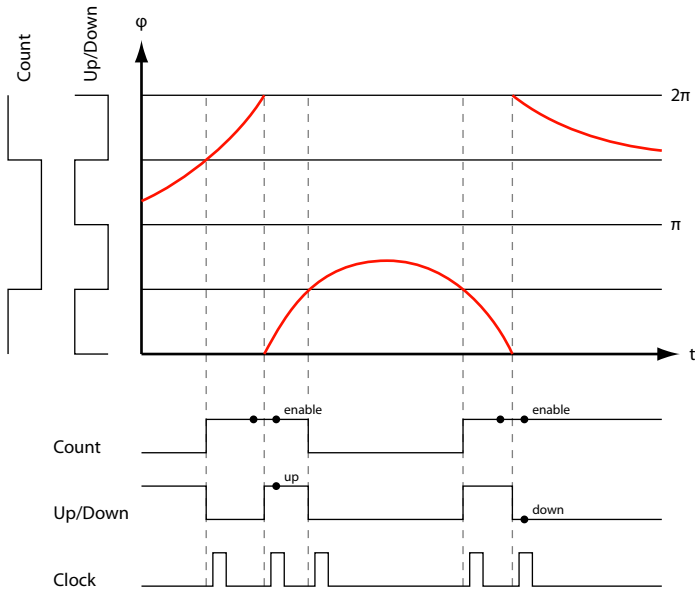


Figure 3.8: Control signals for the integer fringe counter. Cnt: count enable, UD: up/down, CCK: counter clock.

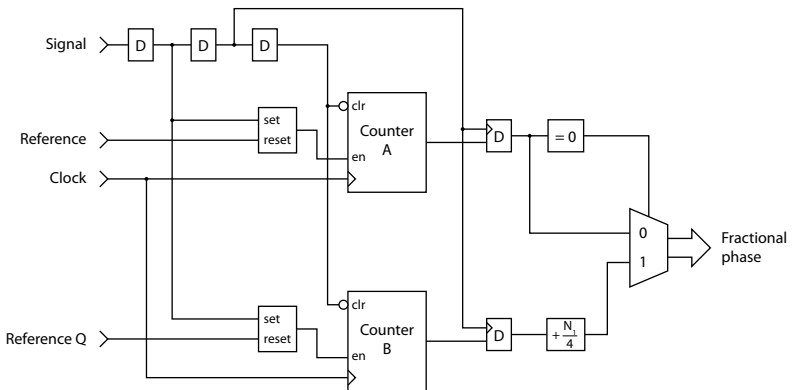


Figure 3.9: Principle of the instantaneous phasemeter, fractional part. Reference: reference signal, Reference Q: reference signal in quadrature, Signal: probe signal, Clock: 200 MHz clock, Counter A: main counter, Counter B: quadrature counter.

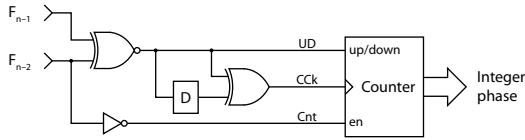


Figure 3.10: Principle of the instantaneous phasemeter, integer part. F_{n-1} , F_{n-2} : two MSBs of the fractional phase, Counter: integer fringe counter, UD: count direction up/down, CCK: counter clock, Cnt: counter enable.

counter is then compensated by adding $N_1/4$ to it. If the value of counter A is zero, it might mean that the value was read before it was ready. Therefore, the value of counter B is used instead by routing it to the output of the phasemeter by means of a multiplexer.

Figure 3.10 shows the logic diagram of the integer fringe counter. The two most significant bits of the fractional phase, F_{n-1} and F_{n-2} , are used to generate the control signals described earlier: counter enable, clock and direction. The maximum distance to be monitored by the phasemeter is 120 mm (mechanical). With a wavelength of 1319 nm, 18 bits are sufficient to store values up to 173 mm ($2^{18} \times \lambda/2$). For safety, an extra bit was allocated to the integer fringe counter. The output of the digital phasemeter is composed of the integer phase on 19 bits and the fractional phase on 10 bits, resulting in a 29 bit word. The least significant bit (LSB) of this value represents a phase of $2\pi/1024$, corresponding to a distance of 0.64 nm (mechanical).

Maximum speed of the differential delay line

In order that the integer fringe counting works correctly, the fractional phase must not change by more than $\pi/2$ between two measurements. Otherwise, the phase skips a quadrant and the zero crossing is not detected properly. This condition limits the speed for the differential delay line to

$$v_{\max} = \frac{\lambda/4}{T} = 66 \text{ mm/s}, \quad (3.17)$$

where the wavelength is $\lambda = 1.3 \mu\text{m}$ and the time between the measurements is $T = 5 \mu\text{s}$, corresponding to the period of the 200 kHz.

3.2.3 Averaging of phase data

The resolution of the phasemeter can be improved by averaging its output over multiple measurements. For ideal signals, the phase resolution is given by the frequency of the clock signal

$$\delta\phi_{\text{ideal}} = 2\pi \frac{f}{f_c} = \frac{2\pi}{N_1}. \quad (3.18)$$

Introducing the error due to the noise in the signal leads to a phase resolution for a single measurement of

$$\delta\phi_{\text{single}} = \sqrt{\frac{4\pi^2}{N_1^2} + \frac{1}{\text{SNR}}}. \quad (3.19)$$

In the case of a phasemeter averaging data on $N = Tf$ independent measurements, the error introduced by the limited SNR is reduced by a factor of \sqrt{Tf} . The error due to the clock frequency, however, is a rounding error which is always the same for a given phase. It is therefore not reduced by averaging

$$\delta\phi_{\text{avg}} = \sqrt{\frac{4\pi^2}{N_1^2} + \frac{1}{Tf \text{ SNR}}}. \quad (3.20)$$

Another benefit of on-board averaging is that it reduces the data rate at the output of the phasemeter by a factor N and therefore reduces the load on the local control unit (LCU) to acquire and process data.

In order to average data over several measurements, the phasemeter must sum and divide them by the number of samples. However, division by an arbitrary number is not easily implemented in the programmable logic used to build the phasemeter. For this reason, the phasemeter prototype only supported averaging on a number of samples that was a power of two, because the division then reduced to shifting the bits of the summed phase by $\log_2 N$ positions.

For the final version of the phasemeter, averaging over an arbitrary number of samples was required. Using a digital signal processing board was considered but it added too much complexity to the system. Therefore, the averaging operation has been split between the phasemeter and the LCU in charge of reading the phasemeter output. The phasemeter adds the instantaneous phase values and counts the number of samples and the LCU performs the division.

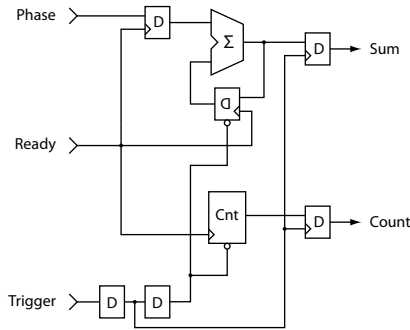


Figure 3.11: Principle of the phase adder. Σ : adder, Cnt: sample counter, D: flip-flops, Phase: integer and fractional phase, Ready: a new phase value is ready, Trigger: end of the current averaging period and start of the next one.

Figure 3.11 shows the principle of the phase adder. When a new phase measurement becomes available, a Ready signal is received from the instantaneous phasemeter. The adder adds the new values for the integer and fractional phase to the previous value of the sum and the sample counter is incremented. When a trigger signal is received at the end of the averaging period, the output latches are loaded with the current values of the summed phase and the sample counter and the adder latch are reset.

The integration time for the averaged phase ranges from $125 \mu\text{s}$ (8 kHz) to 2 s (0.5 Hz), corresponding to a number of samples between 25 and 400000. The width of the sample counter must therefore be at least 19 bits ($\log_2 400000 = 18.6$) and the width of the adder 48 bits ($29 + 19$).

3.2.4 Error compensation fringe counter

Figure 3.12 shows the principle of the error compensation fringe counter. It consists of two digital counters, one for the signal and one for the reference, and a subtractor that computes the difference N_{FC} between the value of the two counters. The variation δL_2 of the OPD of the reference interferometer is then calculated from Eq. (2.17)

$$\delta L_2 = \frac{c}{2\nu} N_{FC}. \tag{3.21}$$

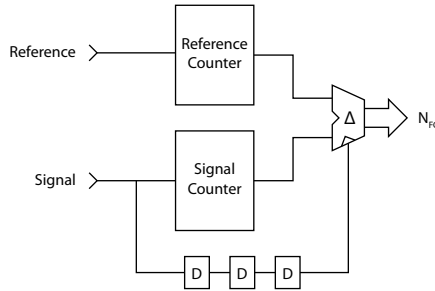


Figure 3.12: Error compensation fringe counter. D: flip-flops, Δ : subtractor.

3.2.5 Status registers

In addition to the summed phase value, the number of samples and the error compensation fringe counter value, some status information was added to the data provided by the phasemeter. This information includes:

- The dc level of each photodetector (4×8 bits);
- Whether the heterodyne signals are present (4 bits);
- Whether the reference and probe superheterodyne signals are present (2 bits);
- Whether there was an overflow of the instantaneous phasemeter or of the error compensation fringe counter (2 bits);
- Whether a trigger or a reset signal was detected (2 bits).

For the dc level of the photodetectors, four Maxim MAX152 8-bit analogue to digital converters were used. For the detection of the heterodyne signals, a frequency counter was implemented in four Microchip PIC12 8-bit microcontrollers. The heterodyne signal is considered present if its frequency is comprised within the 110 kHz bandwidth specified for the input bandpass filters.

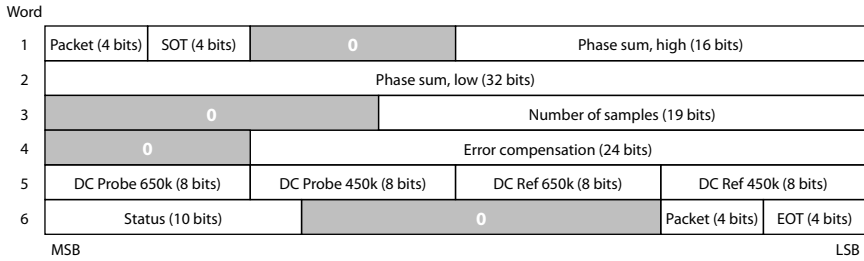


Figure 3.13: Data transfer packet.

3.2.6 Data transfer

The interface between the phasemeter and the LCU is a 32-bit digital I/O board. The data from the phasemeter must therefore be transmitted in a packet of several words. Figure 3.13 shows how the data was distributed over a packet of six 32-bit words.

In order to make sure that all packets were acquired by the LCU and that the acquisition is synchronised with the phasemeter, two control bytes, named Start of Block (SOB) and End of Block (EOB) respectively, were added to the beginning of the first and the end of the last words of the packet. The first four bits contain the packet number, ranging from 0 to 15 and incremented for each packet transferred. The last four bits have fixed values.

Data integrity is checked by ensuring that:

- The packet number is the same for SOB and EOB;
- The last four bits of SOB and EOB have the correct values;
- The packet number is the number of the previous packet plus one.

Chapter 4

Frequency stabilisation of a Nd:YAG laser

4.1 Frequency noise of the laser

The frequency noise of the laser was measured using two different techniques. Long-term frequency fluctuations were measured by monitoring the beat frequency between two free-running lasers of the same model and the noise at higher frequencies was measured by means of an interferometer with a very large optical path difference, using a 1 km fibre delay.

4.1.1 Measurement of the beat frequency

Figure 4.1 shows the set-up used to monitor the beat frequency between the two free-running lasers. The laser beams were combined using a fibre coupler. The beat frequency was detected with a high-speed photodetector (Newport) and measured with a frequency counter (HP53131). The integration time was 100 ms and the sampling rate 1 Hz.

The power spectral density (PSD) of the the frequency noise of an individual laser was deduced from these measurements by dividing by two the PSD in Hz^2/Hz of the beat frequency measurement. Figure 4.2 shows the measurement of the beat frequency over one hour and the deduced PSD for a single laser.

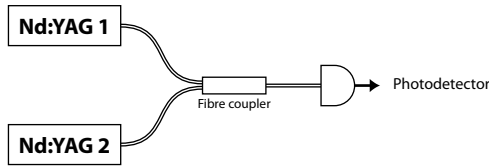


Figure 4.1: Set-up for the measurement of the beat frequency between two free-running lasers.

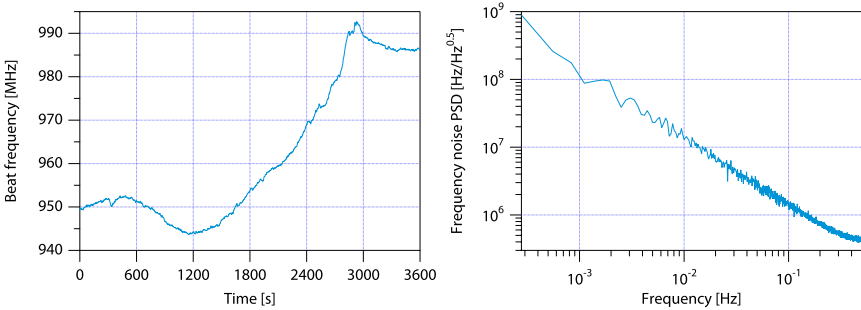


Figure 4.2: Beat frequency measurement for the free-running lasers (left) and deduced frequency noise PSD for a single laser (right). One can see that the frequency noise exhibits a behaviour close to $1/f$ noise.

4.1.2 Measurements at large OPD

Figure 4.3 shows the set-up used to measure the frequency noise of the laser at higher frequencies using the PRIMA phasemeter (see chapter 3, Fig. 3.1). The main interferometer had a large OPD made with a length of fibre of 1 km. A second interferometer was used for the reference signal. In order to monitor the individual OPD of the interferometer, the 450 kHz signal was monitored at 50 kHz over 2 s using the PRIMA phasemeter. An electrically generated signal common to the reference and probe was used for the 650 kHz channel.

Figure 4.4 shows the phase measurement and the PSD of the phase fluctuations. It can be shown [4] that the relation between the PSD of the instantaneous phase fluctuations $S_{\Delta\phi_t}(f)$ and the PSD of the laser frequency fluctuations $S_{\delta\nu}(f)$ is

$$S_{\Delta\phi_t}(f) = 4\pi^2\tau^2 S_{\delta\nu}(f) \left(\frac{\sin \pi f \tau}{\pi f \tau} \right)^2, \quad (4.1)$$

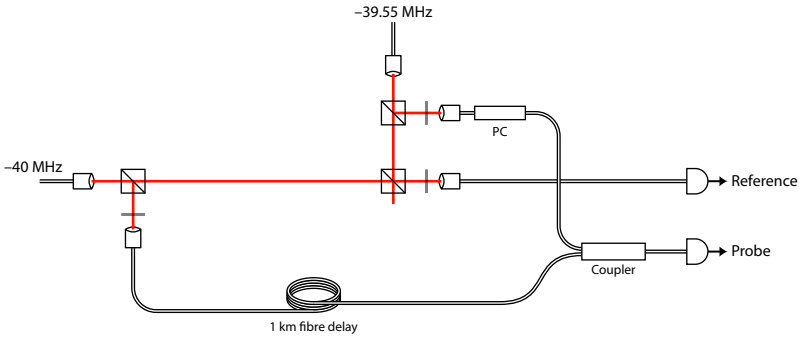


Figure 4.3: Set-up for the measurement of the frequency noise at higher frequencies by means of an interferometer with a very large OPD. PC: polarisation controller.

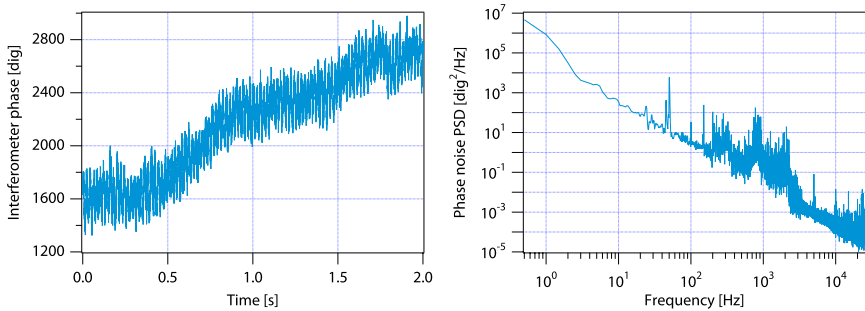


Figure 4.4: Phase measurement at large OPD (left) and PSD of the signal (right). 1 dig = $2\pi/1024$.

where $\tau = \text{OPD}/c$ is the interferometric delay. However, the instantaneous phase can never be observed physically, because of the finite detection bandwidth. Integrated phase fluctuations have therefore to be considered.

The measured phase fluctuations are given by a time averaged value of the instantaneous phase fluctuations during the observation time T

$$\Delta\phi_{\tau,T}(t) = \frac{1}{T} \int_{t-T}^t \Delta\phi_T(t') dt'. \quad (4.2)$$

This averaging introduces a factor $\left(\frac{\sin \pi f T}{\pi f T}\right)^2$ which, if the interferometric delay is much smaller than the integration time, dominates over $\left(\frac{\sin \pi f \tau}{\pi f \tau}\right)^2$. Thus, the PSD of the phase fluctuations becomes

$$S_{\Delta\phi_{\tau,T}}(f) = 4\pi^2\tau^2 S_{\delta\nu}(f) \left(\frac{\sin \pi f T}{\pi f T}\right)^2. \quad (4.3)$$

Assuming that the phase noise measured in Fig. 4.4 is mainly caused by the laser frequency noise spectrum, we can deduce from Eq. (4.3) the power spectral density of the laser frequency fluctuations. For these measurements, the integration time T was of $20 \mu\text{s}$ and the interferometric delay τ is given by OPD/c , where $\text{OPD} = 1.5 \text{ km}$ for a 1 km fibre delay, since the index of refraction of the fibre is about 1.5.

Figure 4.5 shows the frequency noise spectrum of the laser estimated from the beat frequency and the large OPD measurements. A white noise level was assumed above 10 kHz , but the $1/f$ part may still be present until higher frequencies.

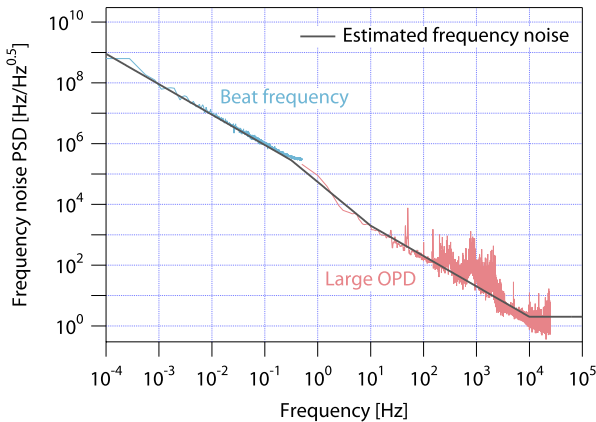


Figure 4.5: Estimated frequency noise spectrum of the laser.

4.1.3 Required frequency noise spectrum

The variance of the measured phase fluctuations $\langle \Delta\phi_{\tau,T}^2 \rangle$ is obtained by using the Parseval relation, which gives

$$\langle \Delta\phi_{\tau,T}^2 \rangle = \int_0^{\infty} S_{\Delta\phi_{\tau,T}}(f) df. \quad (4.4)$$

Assuming as an approximation a white frequency noise within the detection bandwidth for the stabilized laser, i.e. $S_{\delta\nu}(f) = C_0$, for $f < B = 1/2T$, we have

$$\langle \Delta\phi_{\tau,T}^2 \rangle \approx 2\pi^2 C_0 \frac{\tau^2}{T} = 4\pi^2 C_0 \tau^2 B. \quad (4.5)$$

To achieve the desired accuracy of 5 nm the maximal phase variations must be less than $2\pi/132$. Therefore, the standard deviation σ_ϕ must be less than $2\pi/400$ (three sigma). Using Eq. (4.5), we see that the value for C_0 must fulfil the condition

$$C_0 < \frac{\sigma_\phi^2}{4\pi^2 \tau^2 B}. \quad (4.6)$$

For $\tau = 120 \text{ mm}/c = 0.4 \text{ ns}$ and $B = 8 \text{ kHz}$, we see that $C_0 < 5 \times 10^9 \text{ Hz}^2/\text{Hz}$. The power spectral density of the remaining frequency fluctuations must therefore be less

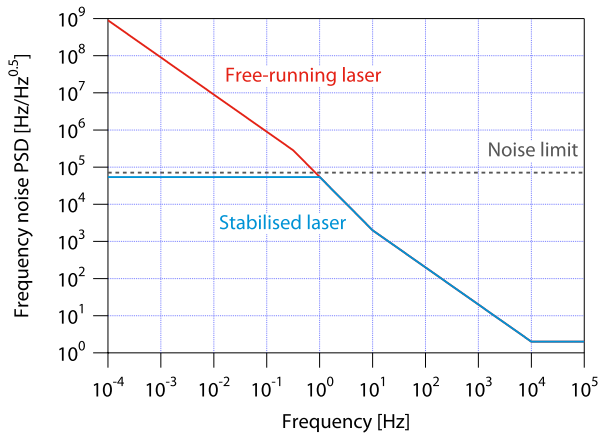


Figure 4.6: Required frequency noise spectrum for the stabilised laser.

than $5 \times 10^9 \text{ Hz}^2/\text{Hz}$ (or $7.1 \times 10^4 \text{ Hz}/\text{Hz}^{0.5}$) for frequencies $f < 8 \text{ kHz}$. The power spectral density shown in Fig. 4.6 allows therefore to fulfil this requirement. As it can be seen, the cut-off frequency of the regulator does not need to be higher than 1 Hz.

4.2 Absolute stabilisation

4.2.1 Absolute frequency references

The tunable range on the 1.3 μm Nd:YAG laser is 50 GHz, corresponding to wavelengths between 1319 and 1319.3 nm. Table 4.1 shows a list of atomic or molecular frequency references with absorption lines close to this range that may be suitable for absolute frequency stabilisation [5].

However, none of these materials are very convenient, either requiring a very long absorption path (up to 10 m to reach a few tens of per cent absorption) or being dangerous and causing handling difficulties.

Gas	Wavelength [nm]	Comments
Carbon Dioxide	1311.8–1320	Very weak lines.
Water vapour	1280–1320	Very weak lines.
Hydrogen Fluoride	1278–1321.2	Highly corrosive.
Hydrogen Sulphide	1280–1320	Toxic.
Nitrate	1315–1320	Complex spectrum, maybe no absorption line within the laser range.
Methane	1312–1320	No absorption line within the laser range.

Table 4.1: Atomic or molecular frequency references with absorption lines within 1319–1319.3 nm.

Second-harmonic	Fundamental	Transition
659.588 nm	1319.176 nm	P(49)6-6
659.570 nm	1319.140 nm	R(55)6-6
659.549 nm	1319.098 nm	P(48)6-6
659.531 nm	1319.062 nm	R(54)6-6
659.529 nm	1319.059 nm	P(111)5-5

Table 4.2: Iodine absorption lines within the tuning range of the Nd:YAG laser.

4.2.2 Stabilisation of the second-harmonic wavelength on iodine

Another technique, first reported by Arie et al. [6], is to generate the second-harmonic of the Nd:YAG laser (at 659.5 nm) and stabilise it on iodine. Iodine is a good candidate for laser stabilisation as its absorption lines are well known and not much subject to temperature drifts (about 10 kHz/°C).

There are ten absorption lines in iodine within the tuning range of the laser. The five strongest ones are shown in table 4.2. The transition used by Arie et al. was P(48)6-6. An iodine cell of length 13 cm was heated to 57°C, leading to an absorption of about 25% for a Doppler-broadened width of 800 MHz. This is the technique that has been retained for the stabilisation of the laser for the PRIMA metrology.

4.2.3 Centre-of-fringe locking

The stabilisation principle called centre-of-fringe locking [7, 8] consists of using the first derivative of the transmission of the frequency reference as the frequency discriminant.

Figure 4.7 shows the transmission of an absorption line, as well as its first derivative. The absorption line is described in a good approximation by a Lorentzian line shape

$$T(\nu) = 1 - A_{\max} \frac{(\Delta\nu/2)^2}{(\nu - \nu_0)^2 + (\Delta\nu/2)^2}, \quad (4.7)$$

where A_{\max} is the absorption coefficient of the line, $\Delta\nu$ the linewidth (FWHM) and ν_0 the centre frequency. One can see that the derivative is zero at the centre frequency ν_0

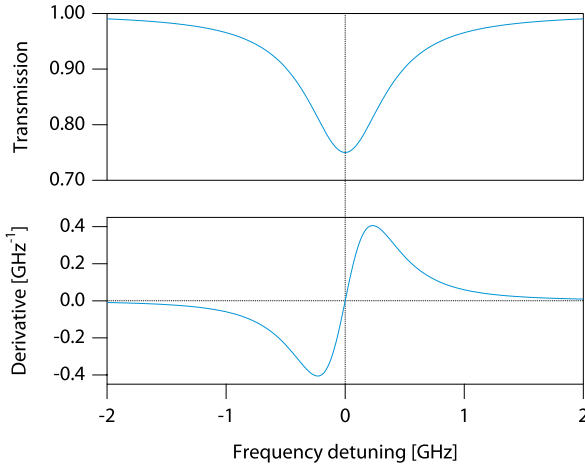


Figure 4.7: An absorption line approximated by a Lorentzian shape and its first derivative.

and changes sign with $(\nu - \nu_0)$, making it a convenient error signal for the feedback loop of the frequency stabilisation.

It is possible to obtain an error signal proportional to the derivative of the absorption line by modulating the frequency of the laser light

$$\nu_\ell(t) = \nu + \nu_{\text{FM}} \sin(2\pi ft), \quad (4.8)$$

where ν_ℓ is the frequency of the modulated laser light, ν_{FM} the frequency excursion and f the modulation frequency. Assuming a monochromatic wave, the transmitted light is given by

$$P_{\text{out}}(\nu_\ell) = P_{\text{in}} T(\nu_\ell), \quad (4.9)$$

where P_{in} is the power of the incident beam. By approximating $T(\nu_\ell)$ with a first-order Taylor series around the average frequency ν , the transmitted power becomes

$$P_{\text{out}}(t) = P_{\text{in}} [T(\nu) + T'(\nu) \nu_{\text{FM}} \sin(2\pi ft)], \quad (4.10)$$

where $T'(\nu)$ is the first derivative of the transmission curve. The sinusoidal function at frequency f is thus proportional to the first derivative of the transmission function.

The stabilisation principle is shown in Fig. 4.8. Synchronous detection is used to measure the component at frequency f of the transmitted power, resulting in the error signal pro-

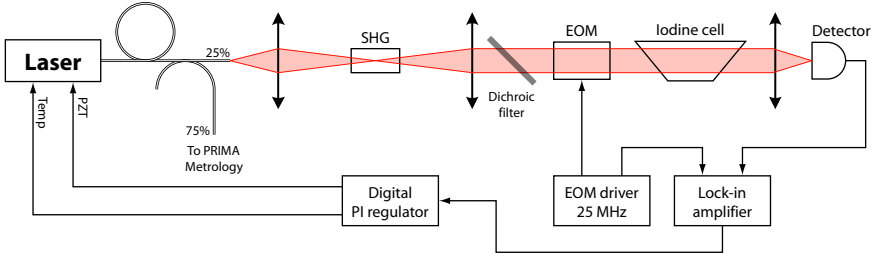


Figure 4.8: Stabilisation principle. SHG: second harmonic generation crystal, EOM: electro-optic modulator.

portional to $T'(v)$. The frequency modulation is achieved using an external frequency or phase modulator. From Eq. (4.7), we can show that the slope of the frequency discriminant is

$$S_{FM} = T''(v_0) v_{FM} = \frac{8A_{\max}}{\Delta v^2} v_{FM}, \quad (4.11)$$

assuming a frequency excursion smaller than the linewidth. We note that this technique is insensitive to the laser power fluctuations and to the change of the absorption coefficient of the cell. In addition, synchronous detection allows to work at relatively high frequencies ($f > 10$ kHz), where the $1/f$ noise of electronic components is no longer dominant.

Required optical power in the second harmonic

Assuming an input power P_{in} of 300 nW, which is a reasonable minimum for what can be expected after second harmonic generation, an absorption coefficient A_{\max} of 25% and a linewidth Δv of 800 MHz, one can calculate the minimum detectable frequency drift δv , using a commercially available photodetector (Analog Modules, model no 712A-2) with a voltage sensitivity S_{VP} of $0.7 \text{ V}/\mu\text{W}$ and a noise-equivalent power (NEP) of $2.1 \text{ pW}/\sqrt{\text{Hz}}$. The voltage sensitivity at the output of the photodetector will be

$$S_{VF} = P_{in} S_{FM} S_{VP} = P_{in} \frac{8A_{\max}}{\Delta v^2} v_{FM} S_{VP} = 0.052 \text{ V/GHz}. \quad (4.12)$$

The detection bandwidth does not need to be very high, since the cut-off frequency of the regulator does not need to be higher than 1 Hz. Therefore a cut-off frequency of 100

Hz for the lock-in amplifier is high enough. For a bandwidth B of 100 Hz, the voltage noise is

$$\sigma_v = \text{NEP } S_{\text{VP}} \sqrt{B} = 0.015 \text{ mV}. \quad (4.13)$$

The signal-to-noise ratio of the detected signal for a frequency drift δv is

$$\text{SNR}_{\text{ac}} = \frac{(S_{\text{VF}} \delta v)^2 \langle \cos^2(2\pi ft) \rangle}{\sigma_v^2} = \frac{1}{2} \frac{(S_{\text{VF}} \delta v)^2}{\sigma_v^2}. \quad (4.14)$$

The minimal detectable frequency drift δv_{min} is the value for which $\text{SNR}_{\text{ac}} = 1$. We find a value of $\delta v_{\text{min}} = 400 \text{ kHz}$, which is well below the required 2 MHz frequency stability. Synchronous detection should therefore allow to get the desired stability even for a second-harmonic power as low as 300 nW and a detection bandwidth of $B = 100 \text{ Hz}$.

4.3 Second-harmonic generation

Second-harmonic generation uses the nonlinear dielectric properties of certain classes of crystals to generate a wave whose frequency is the double of that of the incoming wave [9, 10, 11]. The optical electric field \mathbf{E} produces a polarisation \mathbf{P} with a linear and a quadratic response

$$P_i = \epsilon_0 \chi_{\text{ik}}^{(1)} E_k + \epsilon_0 \chi_{\text{ikn}}^{(2)} E_k E_n \quad i = x, y, z. \quad (4.15)$$

where $\chi_{\text{ik}}^{(1)}$ and $\chi_{\text{ikn}}^{(2)}$ are respectively the linear and second-order nonlinear optical susceptibilities of the crystal. Summations over repeated indices are assumed.

This nonlinear response allows an exchange of energy between electromagnetic fields of different frequencies. In the case of second-harmonic generation, this effect is used to transfer part of the energy of a wave of frequency ω to its second-harmonic at 2ω .

4.3.1 Birefringent phase matching

The general case for describing second-harmonic generation is three-wave mixing. The incoming beam is represented by two waves of wave vectors \mathbf{k}_1 and \mathbf{k}_2 and of frequency ω

and the outgoing beam by a wave of wave vector \mathbf{k}_3 and of frequency 2ω . The phase matching condition must be fulfilled in order for second-harmonic light to be generated

$$\mathbf{k}_3 = \mathbf{k}_1 + \mathbf{k}_2. \quad (4.16)$$

If the three waves propagate in the same direction, it becomes

$$2n_3(2\omega) = n_1(\omega) + n_2(\omega). \quad (4.17)$$

Since the nonlinear medium is dispersive, this condition is in general not fulfilled. However, by taking advantage of the birefringence of the crystal, phase matching can often be achieved by choosing an appropriate polarisation and direction of the incoming beam relative to the crystal axes. This is called birefringent phase matching. Two types of phase matching are generally employed. They are described here for a uniaxial crystal with an ordinary index of refraction n_o and an extraordinary index n_e .

In **type I** phase matching, the fundamental and harmonic are orthogonally polarised. The input is an extraordinary beam for which the index of refraction is $n_1 = n_2 = n_e^\omega(\theta)$, where θ is the angle between the axes of the crystal and the direction of propagation. The output is an ordinary beam for which the index of refraction is $n_3 = n_o^{2\omega}$. The phase matching condition is

$$\frac{1}{(n_o^{2\omega})^2} = \frac{1}{(n_e^\omega(\theta))^2} = \frac{\cos^2 \theta}{(n_o^\omega)^2} + \frac{\sin^2 \theta}{(n_e^\omega)^2}. \quad (4.18)$$

In **type II** phase matching, the incoming wave is polarised at 45 degrees relative to the axes of the crystal (Fig. 4.9). The input is therefore the combination of an ordinary and an extraordinary beam, for which the index of refraction is $n_1 = n_e^\omega(\theta)$ and $n_2 = n_o^\omega$, respectively. The output can be either an ordinary or an extraordinary beam. In the case of an ordinary beam, the refractive index is $n_3 = n_o^{2\omega}$. The phase matching condition is

$$2n_o^{2\omega} = n_e^\omega(\theta) + n_o^\omega. \quad (4.19)$$

4.3.2 Conversion efficiency

The first approach considered was to use type II phase matching in a KTP crystal to generate the second harmonic light needed for the laser stabilisation.

The expected conversion efficiency in KTP can be calculated using coupled waves theory. The solutions without perturbation are the ordinary (\mathbf{A}_1) and extraordinary (\mathbf{A}_2)

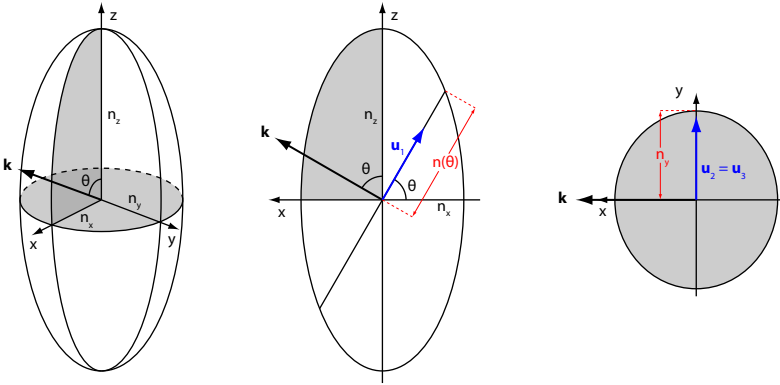


Figure 4.9: Ellipsoid of the refractive indices for type II phase matching.

components of the fundamental beam and the extraordinary harmonic beam (\mathbf{A}_3)

$$\begin{aligned}
 \mathbf{A}_1(\mathbf{r}, t) &= \mathbf{U}_1(x, y) e^{i(\omega t - \beta_1 z)} \\
 \mathbf{A}_2(\mathbf{r}, t) &= \mathbf{U}_2(x, y) e^{i(\omega t - \beta_2 z)} \\
 \mathbf{A}_3(\mathbf{r}, t) &= \mathbf{U}_3(x, y) e^{i(2\omega t - \beta_3 z)},
 \end{aligned} \tag{4.20}$$

where $\beta_m = \frac{n_m \omega_m}{c}$. Following Fig. 4.9, the polarisation vectors of the three beams are

$$\mathbf{u}_1 = \begin{pmatrix} \cos \theta \\ 0 \\ \sin \theta \end{pmatrix} \quad \mathbf{u}_2 = \begin{pmatrix} 0 \\ 1 \\ 0 \end{pmatrix} \quad \mathbf{u}_3 = \begin{pmatrix} 0 \\ 1 \\ 0 \end{pmatrix}, \tag{4.21}$$

where θ is the phase matching angle, and the refractive indices are

$$n_1 = n_e^\omega(\theta) = n^\omega(\theta) \quad n_2 = n_o^\omega = n_y^\omega \quad n_3 = n_o^{2\omega} = n_y^{2\omega}. \tag{4.22}$$

The general solution, with perturbation, to the coupled waves equation is a combination of the solutions without perturbation

$$\mathbf{E}(\mathbf{r}, t) = \frac{1}{2} \sum_{m=1}^3 [a_m(z) \mathbf{A}_m(\mathbf{r}, t) + cc]. \tag{4.23}$$

In this case, the perturbation is the nonlinear part of the polarisation

$$\mathbf{p}_i = \epsilon_0 \chi_{ikn}^{(2)} E_k E_n. \tag{4.24}$$

The coupled waves equation for the second harmonic is

$$\frac{da_3}{dz} = \frac{i\mu_0}{2\Gamma W_3 \beta_3} e^{i\beta_3 z} \int dx dy \int_T dt \mathbf{U}_3^*(x, y) e^{-i\omega_3 t} \cdot \ddot{\mathbf{p}}(\mathbf{r}, t). \quad (4.25)$$

In this particular case, the propagation direction and the polarisations have been chosen for the phase matching condition to be fulfilled. In addition, the following assumptions are made:

- $\frac{1}{W_m} \int dx dy \mathbf{U}_m^*(x, y) = \mathbf{u}_m$;
- \mathbf{u}_3 has only a y component;
- The phase matching condition only preserves terms in $a_1 a_2$, containing $\chi_{yyx}^{(2)}$ and $\chi_{yyz}^{(2)}$;
- In KTP, $\chi_{yx}^{(2)}$ is (nearly) zero.

Equation (4.25) for the second harmonic then becomes

$$\frac{da_3}{dz} = -\frac{2i\omega}{n_3 c} \chi_{yyz}^{(2)} a_1 a_2 \sin \theta. \quad (4.26)$$

In order to calculate the conversion efficiency, intensities must be introduced by

$$I_m = \frac{1}{2} \left(\frac{\epsilon_0}{\mu_0} \right)^{\frac{1}{2}} n_m |a_m|^2. \quad (4.27)$$

I_1 and I_2 are half of the intensity I_f of the fundamental beam each and I_3 is the intensity of the second harmonic

$$I_1 = I_2 = \frac{1}{2} I_f \quad I_3 = I_h. \quad (4.28)$$

Moreover, since the conversion efficiency is very small, the amplitude of the fundamental can be assumed to be constant over the length of the crystal, leading to

$$a_1(z) = a_{10} \quad a_2(z) = a_{20}. \quad (4.29)$$

Therefore

$$a_3(z) = -\frac{2i\omega}{n_3 c} \chi_{yyz}^{(2)} a_{10} a_{20} \sin \theta z, \quad (4.30)$$

and the conversion efficiency η is calculated as

$$\begin{aligned}\eta &= \frac{I_3}{I_1 + I_2} \\ &= \frac{n_3 |a_3(\ell)|^2}{n_1 |a_{10}|^2 + n_2 |a_{20}|^2} \\ &= 2 \left(\frac{\mu_0}{\epsilon_0} \right)^{\frac{3}{2}} \frac{\omega^2 \ell^2}{n^3} \left(\epsilon_0 \chi_{yyz}^{(2)} \sin \theta \right)^2 I_f,\end{aligned}\tag{4.31}$$

where ℓ is the length of the crystal and $n^3 = n_1 n_2 n_3$.

The indices of refraction of KTP were calculated using the Sellmeier equation [12]

$$n_i^2(\lambda) = a_i + \beta_i \Delta T^2 + \frac{b_i + \delta_i \Delta T^2}{\lambda^2 - c_i + \phi_i \Delta T^2} - [d_i + \rho_i \Delta T^2] \lambda^2.\tag{4.32}$$

At room temperature, the temperature-dependant coefficients can be left out of the equation

$$n_i^2(\lambda) = a_i + \frac{b_i}{\lambda^2 - c_i} - d_i \lambda^2.\tag{4.33}$$

Using the coefficients from Tab. 4.3, the indices of refraction of KTP at 1319 nm and 659.5 nm were calculated as

$$\begin{array}{lll}n_x^\omega = 1.7339 & n_y^\omega = 1.74164 & n_z^\omega = 1.82153 \\ n_x^{2\omega} = 1.76072 & n_y^{2\omega} = 1.77026 & n_z^{2\omega} = 1.85919.\end{array}$$

Coefficient	x	y	z
a_i	3.0065	3.0333	3.3134
b_i	0.03901	0.04154	0.05694
c_i	0.04251	0.04547	0.05657
d_i	0.01327	0.01408	0.01682

Table 4.3: Sellmeier equation parameters for KTP.

One can see that there is a small difference of index between the x and y directions, and therefore KTP is not really a uniaxial crystal. However, it was treated as uniaxial for simplification, the much higher index n_3 playing the role of the extraordinary index n_e .

The phase matching condition $\beta_1 + \beta_2 - \beta_3 = 0$ gives

$$n^\omega(\theta) + n_y^\omega - 2n_y^{2\omega} = 0. \quad (4.34)$$

With $n^\omega(\theta)$, the equation of the ellipsoid of refraction indices for the extraordinary beam, can be solved for θ

$$\left(\frac{n^\omega(\theta) \cos \theta}{n_x}\right)^2 + \left(\frac{n^\omega(\theta) \sin \theta}{n_z}\right)^2 = 1. \quad (4.35)$$

It gives the phase matching angle $\theta = 60.4^\circ$.

The nonlinear electric susceptibility for KTP can be found in [13]

$$\begin{aligned} d_{31} &= 6.5 \frac{\text{pm}}{\text{V}} = \chi_{311} = \chi_{113} = \chi_{131} \\ d_{32} &= 5.0 \frac{\text{pm}}{\text{V}} = \chi_{322} = \chi_{223} = \chi_{232} \\ d_{33} &= 13.7 \frac{\text{pm}}{\text{V}} = \chi_{333} \\ d_{34} &= 7.6 \frac{\text{pm}}{\text{V}} = \chi_{332} = \chi_{323} = \chi_{233} \\ d_{35} &= 6.1 \frac{\text{pm}}{\text{V}} = \chi_{331} = \chi_{313} = \chi_{133}. \end{aligned} \quad (4.36)$$

For a crystal of a length of 8 mm, with the beam focussed to a diameter $2w_0$ of $60 \mu\text{m}$, as recommended in [10] so that the Rayleigh distance z_0 is equal to half the length of the crystal, the calculated conversion efficiency η was of 3.1×10^{-5} , leading to an expected output power of $1.55 \mu\text{W}$ for an input power of 50mW .

However, the experimental results did not match this estimation. With an input power of 60mW , only 17nW of second harmonic light were obtained, corresponding to an efficiency of 3×10^{-7} . The cause of this reduced efficiency was identified to be birefringent walk-off.

4.3.3 Birefringent walk-off

In anisotropic materials, the electric field \mathbf{E} is not parallel to the electric induction \mathbf{D} (Fig. 4.10). As a result, the wave vector \mathbf{k} (perpendicular to \mathbf{D}) is not parallel to the

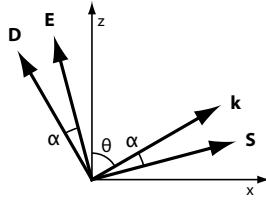


Figure 4.10: Birefringent walk-off.

Poynting vector \mathbf{S} (perpendicular to \mathbf{E}). This is known as birefringent walk-off. In the case of second harmonic generation with Type II phase matching, the two components of the fundamental beam separate spatially because of this, and the interaction length (and therefore the conversion efficiency, which is proportional to the square of the interaction length) is reduced.

The relation between \mathbf{D} and \mathbf{E} is given by

$$D_i = \epsilon_0 \epsilon_{ik} E_k, \tag{4.37}$$

ϵ is related to the refractive indexes of the material by

$$\epsilon = \begin{pmatrix} n_x^2 & 0 & 0 \\ 0 & n_y^2 & 0 \\ 0 & 0 & n_z^2 \end{pmatrix}. \tag{4.38}$$

Thus we have

$$\mathbf{D} = \begin{pmatrix} D \cos \theta \\ 0 \\ D \sin \theta \end{pmatrix} \quad \mathbf{E} = \frac{D}{\epsilon_0} \begin{pmatrix} \cos \theta / n_x^2 \\ 0 \\ \sin \theta / n_z^2 \end{pmatrix}. \tag{4.39}$$

The walk-off angle α can then be calculated using the relation

$$\cos \alpha = \frac{\mathbf{D} \cdot \mathbf{E}}{|\mathbf{D}||\mathbf{E}|} = \frac{\left(\frac{\cos \theta}{n_x}\right)^2 + \left(\frac{\sin \theta}{n_z}\right)^2}{\sqrt{\frac{\cos^2 \theta}{n_x^4} + \frac{\sin^2 \theta}{n_z^4}}}. \tag{4.40}$$

In KTP, in the conditions described above, the walk-off angle is of 43 mrad, which gives an interaction length of about 1.5 mm for a beam diameter of $2w_0 = 60 \mu\text{m}$.

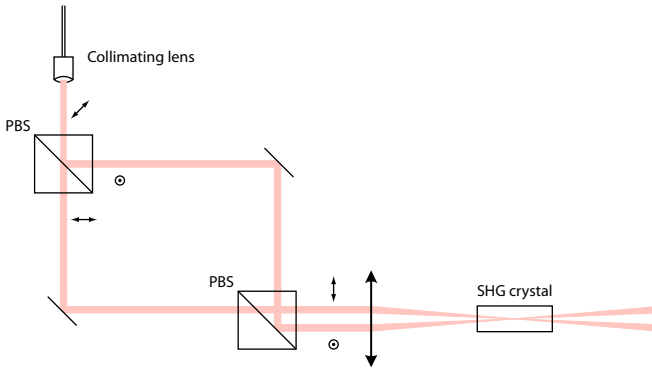


Figure 4.11: Set-up for walk-off compensation.

The efficiency is therefore reduced to 10^{-6} , which is closer to the 3×10^{-7} obtained in laboratory.

A set-up for walk-off compensation was proposed and is depicted on Fig. 4.11. The vertical and horizontal components of the input polarisation are separated using a polarising beam splitter. A shift in the x-direction is introduced and the beams are recombined. Because of the focussing lens, the shift will introduce an angle between the two polarisations that can be used to compensate the walk-off angle.

4.3.4 Quasi-phase matching in periodically-poled crystals

Given the relatively complex set-up required to compensate the walk-off angle and the apparition of periodically-poled nonlinear crystals for quasi-phase matching, the birefringent phase matching approach was abandoned in favour of quasi-phase matching.

Quasi-phase matching takes advantage of the fact that when the phase matching condition is not fulfilled, as long as the phase between the input and the output is less than 180 deg, energy flows from the fundamental to the harmonic frequency. This flow is reversed for phases greater than 180 deg. The coherence length of the crystal is the distance for which the phase is less than 180 deg.

In periodic poling, the axes of the crystal are flipped after each coherence length, which results in a phase change and the energy continues to flow from the fundamental to the harmonic (Fig. 4.12). Periodic poling is achieved by periodic ferroelectric domain

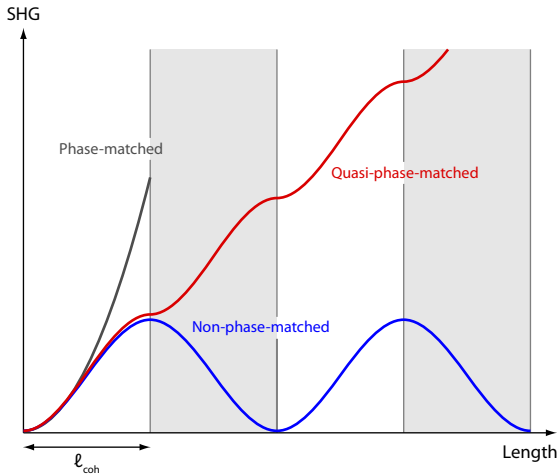


Figure 4.12: Quasi-phase matching.

reversal. In quasi-phase matching, the Poynting vector of all waves has the same direction, which avoids birefringent walk-off problems. Moreover, all waves can have the same polarisation, which grants access to the larger d_{33} nonlinear coefficient which is not accessible with birefringent phase matching.

4.4 Set-up for the laser stabilisation

Figure 4.13 shows the set-up for the laser stabilisation. A quarter of the laser power is taken using a 25/75 polarisation-maintaining fibre coupler. The light is focused into the periodically-poled LiNbO₃ crystal using an aspherical lens and the harmonic beam is collimated with an achromatic lens. At this point, a dichroic filter is used to block the infrared beam and only keep the second harmonic. The beam is modulated in frequency by means of an electro-optic phase modulator and passes through the iodine absorption cell. A second achromatic lens is used to focus the beam onto the photodetector.

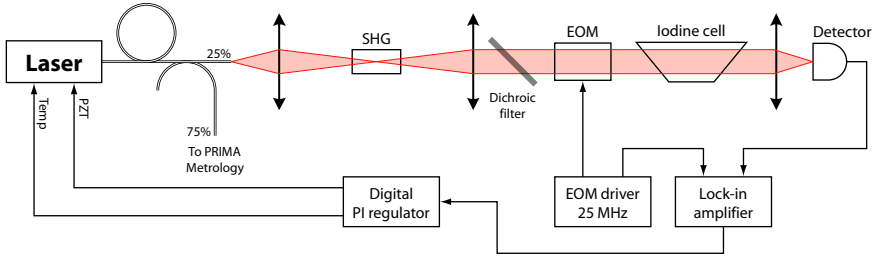


Figure 4.13: Set-up for the laser stabilisation.

4.4.1 Second harmonic generation

The 20 mm long periodically-poled Lithium Niobate crystal was placed in an oven (HC-Photonics OV03145305) whose temperature was regulated by a Newport Omega CN77352-C4 PID controller, in order to optimise the conversion efficiency by matching the period of the periodic poling with the working wavelength. For an optical power of 50 mW in the fundamental beam focussed to a diameter of 51.5 μm and a temperature of 44.5 ± 0.1 $^{\circ}\text{C}$, a second harmonic power of 12 μW was obtained at ESO by Samuel Lévêque and Nicolas Schuhler.

4.4.2 Frequency modulation

An electro-optic modulator was chosen to generate the frequency modulation of the laser beam. Its effect is a modulation of the phase, given by

$$\phi(t) = \phi_0 \sin(2\pi ft), \quad (4.41)$$

where ϕ_0 is the amplitude of the phase modulation and f the frequency of the modulation. This leads to a modulation of the frequency

$$v(t) = v + \frac{1}{2\pi} \frac{d\phi}{dt} = v + f\phi_0 \cos(2\pi ft). \quad (4.42)$$

The frequency excursion depends therefore on the phase modulation amplitude ϕ_0 and the modulation frequency f . Assuming a phase amplitude of π (typical value), the modulation frequency required to obtain a frequency excursion of 80 MHz is 25 MHz.

A New Focus model 4001-M resonant electro-optic phase modulator with its 3363-B driver was used. Resonant phase modulators operate at a single frequency, defined at

manufacturing, but require much lower drive voltages than their non-resonant counterparts. The modulator used in this set-up was driven by a voltage of 16 V.

A limitation of phase modulators is the residual amplitude modulation (RAM). Whereas an ideal phase modulator should not modulate the intensity of the optical beam, a misalignment of the input polarisation relative to the axes of the crystal can result in a slightly elliptical polarisation inside the modulator, which will introduce some level of amplitude modulation. This effect can be minimised by using a collimated beam whose polarisation is properly aligned with the principal axis of the modulator. During the setting-up of the system, the RAM was monitored using the photodetector and minimised by acting on the polarisation and the position of the modulator.

4.4.3 Absorption

A fused silica absorption cell was manufactured by Hellma. It has a length of 150 mm and an aperture of 50 mm, with Brewster-angle windows. It was filled with iodine by the Physikalisch-Technische Bundesanstalt, Braunschweig.

The cell had to be heated to a temperature of 60 °C in order to obtain an internal pressure of about 3.5 Torr. The cell was therefore placed in a cylindrical Aluminium housing with thermo-conductor gel foil to ensure a good thermic contact. Heating bands with a total resistance of 30 Ω were placed on the Aluminium cylinder and the whole was covered with an insulating foil.

A voltage-controlled power supply delivering 1 A at 60 V (KNIEL CUI60.1) was used to heat the cell. A Newport-Omega CN-77352-C4 temperature controller reading the value from a Positive Temperature Coefficient resistor (PTC) placed on the side of the cell.

During the testing of the cell, an absorption of only 7 % was achieved by heating it to 65 °C. Moreover, fluctuations of absorption were observed. It turned out that the fluctuations were due to condensation of the iodine in the cold finger of the cell. After adding heating elements and insulation to the cold finger, absorptions between 25 and 35 % were achieved with temperatures between 60 and 70 °C.

4.4.4 Optical detection

The photodetector used was an Analog Modules model 712A-2. It has a voltage sensitivity of 0.7 V/ μ W and a noise of 2.1 pW/ $\sqrt{\text{Hz}}$. In order to access the highest specified

detection bandwidth of 60 MHz and detect the laser light modulated at 25 MHz, an external reverse bias of 45 V was applied by means of the model 521-1 high voltage bias supply.

4.4.5 Control loop

For the control loop, the intensity at the output of the iodine cell is synchronously detected using a lock-in amplifier. The $(R \cos \theta)$ output of the lock-in amplifier gives the error signal proportional to the first derivative of the absorption lineshape, as depicted on Fig 4.7.

The Nd:YAG laser has two inputs for frequency tuning. The first one controls a Pelletier element that acts on the temperature of the crystal. It has a broad frequency range (about 3.6 V/GHz over 16 GHz without mode hops in the region of the chosen absorption line of iodine) but a large response time (about 5 s). The second one controls a piezoelectric element that induces stress on the crystal, changing the index of refraction and thus the resonance frequency. It has a much smaller response time (130 ms) but also a narrower range (± 30 MHz).

The control loop was designed so that the fast frequency fluctuations are compensated by acting on the piezo input. A Proportional-Integral (PI) controller was used for this purpose. The transfer function of the PI is

$$U = \frac{K_p}{T_i} \left(\frac{1 + T_i s}{s} \right), \quad (4.43)$$

where K_p is the proportional gain and T_i the integration time.

The slower temperature input was used to take care of the low frequency drifts that would otherwise saturate the piezo over time. For this purpose, a Lead/Lag controller was used, taking the output of the PI regulator as its input. Its transfer function is

$$U = G \left(\frac{1 + T_{\text{lag}} s}{1 + T_{\text{lead}} s} \right). \quad (4.44)$$

Table 4.4 summarises the parameters selected for the PI and Lead/Lag control loops. The lag time of the Lead/Lag matching the integration time of the PI. Figure 4.14 shows the frequency noise spectrum of the free-running laser, the transfer function of the control loop and the expected frequency spectrum of the stabilised laser.

PI		Lead/Lag	
K_p	1.1	G	1
T_i	134 ms	T_{lead}	5 s
Loop rate	1 kHz	T_{lag}	134 ms

Table 4.4: Parameters for the PI and Lead/Lag control loops.

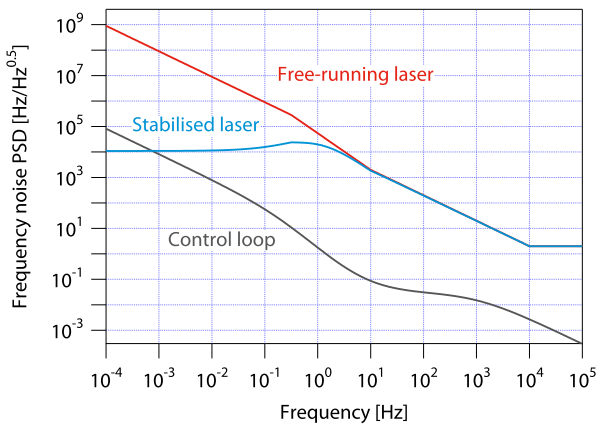


Figure 4.14: Frequency noise spectrum of the free-running laser, transfer function of the control loop and expected frequency spectrum of the stabilised laser.

Chapter 5

Tests of the phasemeter and of the laser stabilisation

5.1 Tests of the phasemeter

5.1.1 Electrical tests of the phasemeter

The electrical tests of the PRIMA phasemeter measured the noise performance of the photodetectors and the analogue boards as well as the correct operation of the digital board.

Characterisation of the photodetectors

As explained in chapter 3.1.2, the bandwidth of the photodetectors was designed to be much higher than the frequency of the detected signals, in order to obtain a phase response as flat as possible at the working frequencies and avoid the introduction of phase shifts when the frequency of the heterodyne signals changes due to the movement of the delay lines.

The bandwidth and noise of the photodetectors were measured using a modulated laser diode at 650 nm and an HP4195A network/spectrum analyser. They all had similar characteristics with a bandwidth of 7.7 MHz and a noise below -128 dBm/Hz, as ex-

pected in the design phase. With the minimum optical power of 20 nW and a detection bandwidth of 55 kHz, this noise level corresponds to a SNR of 55 dB, which is well above the required SNR of 40 dB.

Characterisation of the bandpass filters

The specification for the bandwidth of the input bandpass filters at 450 and 650 kHz was of 110 kHz, allowing for a Doppler shift Δf of the heterodyne frequencies of up to ± 55 kHz corresponding to a velocity of the delay lines v_{OPLmax} of

$$v_{\text{OPLmax}} = \frac{\lambda \Delta f}{2} = \pm 36 \text{ mm/s.} \quad (5.1)$$

The specified bandwidth for the output filters at 200 kHz was of 55 kHz allowing for a maximum velocity of the differential delay line of ± 18 mm/s.

The frequency and phase responses of the bandpass filters were also measured using the network analyser. The bandwidth for the input filters at 450 and 650 kHz was of 150 kHz, allowing for a maximum velocity of the delay lines of ± 49 mm/s and the bandwidth for the output filters at 200 kHz was of 69 kHz, corresponding to a maximum velocity of the differential delay line of ± 23 mm/s.

Moreover, the difference of the phase responses of the 450 and 650 kHz filters, aligned on their centre frequency, was calculated in order to determine the phase shifts introduced by the frequency shift due to the movement of the delay lines (detuning frequency). The result is shown on Fig. 5.1. One can see that the phase difference does not exceed 0.42° ($2\pi/857$), corresponding to a distance error of about 0.8 nm for detuning frequencies between -55 kHz and $+55$ kHz

Measurement of the signal to noise ratio of the analogue boards with full crosstalk

Figure 5.2 shows the set-up used to measure the noise introduced by the analogue boards and the crosstalks between the 450 and 650 kHz channels. Two phase-locked function generators were used to generate signals at 450 and 650 kHz that were superposed using a 50 Ω power splitter and fed to the electric inputs of both channels of the phasemeter. This allows to simulate full crosstalk between the two heterodyne frequencies. The spectrum of the digital superheterodyne signal at 200 kHz was measured at the output of the limiting amplifier.

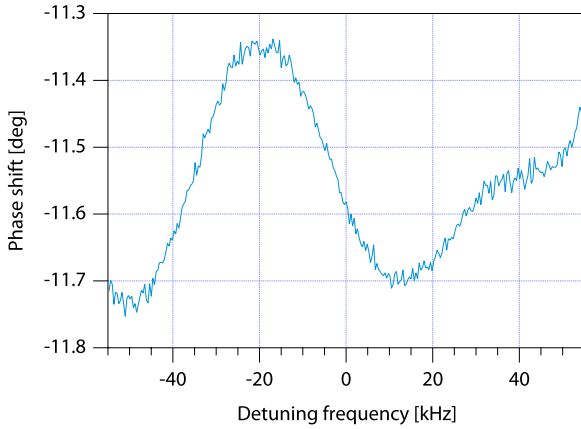


Figure 5.1: Calculated phase shift introduced by the bandpass filters at 450 kHz and 650 kHz.

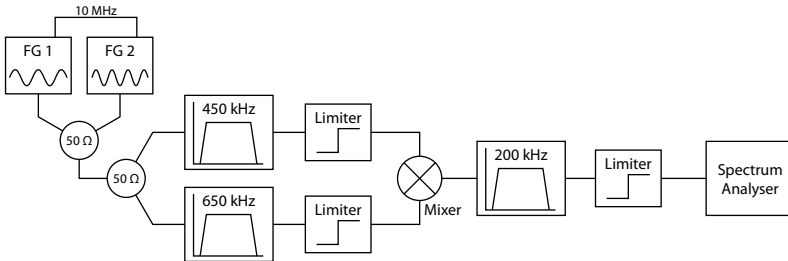


Figure 5.2: Set-up used to measure the SNR of the analogue boards.

The optical power in each arm P_{avg} corresponding to a given input level V_{pp} was calculated from the sensitivity of the photodetectors S , assuming an interference contrast m of 50 %:

$$P_{avg} = \frac{V_{PP}}{2mS}, \tag{5.2}$$

where $S = 1.23 \text{ V}/\mu\text{W}$.

Table 5.1 summarises the SNR measurements. For equivalent optical powers above 7 nW, the SNR for both the reference and probe channels of the phasemeter was above

Input level	Optical power	SNR Ref	SNR Probe
140 mVpp	57 nW	60 dB	62 dB
70 mVpp	28 nW	59 dB	61.5 dB
35 mVpp	14 nW	60.5 dB	60.5 dB
17.5 mVpp	7 nW	60 dB	59.7 dB
0.56 mVpp	0.2 nW	43 dB	43 dB

Table 5.1: SNR in the analogue boards for different input levels.

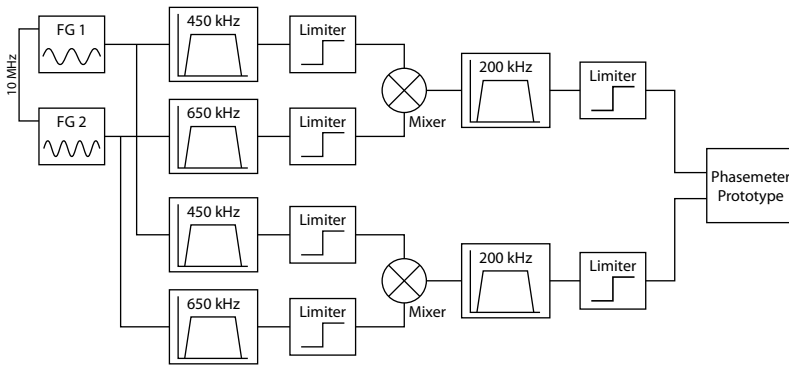


Figure 5.3: Set-up used to measure the phase resolution of the analogue phasemeter.

58 dB. For an equivalent power of 0.2 nW, the SNR was of 43 dB, which is still above the required SNR of 40 dB for an optical power of 20 nW.

Electrical tests with the phasemeter prototype digital board

The phase resolution of the analogue part of the phasemeter was measured using the set-up depicted on Fig. 5.3. Sinusoidal electrical signals at 450 kHz and 650 kHz common to the reference and probe channels were generated using the phase-locked function generators and the mean and rms values of the phase were calculated, for different input levels, on a run of 4000 measurements with a sampling frequency of 200 kHz. Each measurement was averaged over 4 samples by the digital board.

Signal level	Optical power	rms resolution
100 mV _{pp}	42 nW	0.55 digit
75 mV _{pp}	32 nW	0.50 digit
50 mV _{pp}	21 nW	0.61 digit
25 mV _{pp}	11 nW	0.77 digit
17 mV _{pp}	7 nW	0.80 digit
12 mV _{pp}	5 nW	0.86 digit
10 mV _{pp}	4 nW	0.91 digit

Table 5.2: Phase resolution of the analogue phasemeter for different input levels.

Table 5.2 summarises the phase resolution measurements. For an equivalent optical power of 21 nW, the rms resolution was of $2\pi/1678$ (0.61 digit), corresponding to a distance of 0.4 nm. As explained in chapter 2.4, the required resolution for 20 nW is of $2\pi/660$.

5.1.2 Test of accuracy using two-wavelength interferometry

The goal of the test of accuracy was to demonstrate that the phase measured by the phasemeter accurately represents the distance travelled by the delay lines. However, measuring a $2\pi/130$ accuracy over 120 mm using a one-wavelength source at 1319 nm would require a mechanical stability of the set-up of 5 nm and control of the refractive index of air, which is very difficult to achieve in the laboratory.

On the other hand, two-wavelength interferometry allows to generate a synthetic wavelength $\Lambda = c/\Delta\nu$ much longer than the individual optical wavelengths [3, 14]. In this case, it allows to reduce the sensitivity of the measurement while retaining the concept of the test. Using a synthetic wavelength of 200 mm, a mechanical stability of only 0.1 mm is required to demonstrate an accuracy of $2\pi/1000$, which is easily achievable in the laboratory.

Figure 5.4 shows the set-up used for this test. Heterodyne frequency f_1 is generated on the first wavelength λ_1 and heterodyne frequency f_2 on wavelength λ_2 . Therefore, the

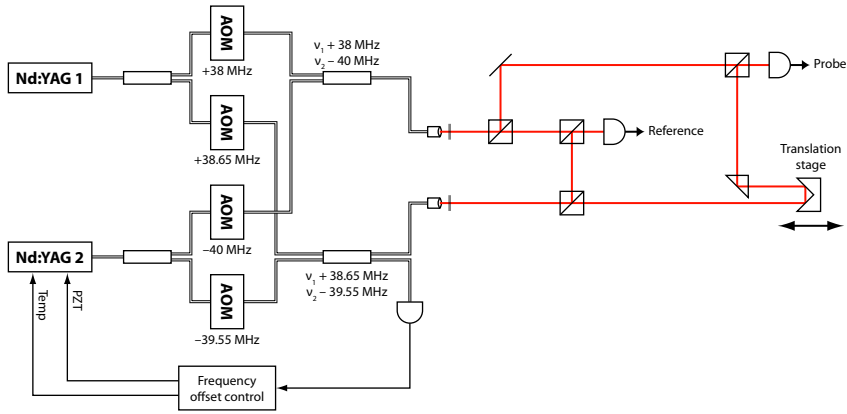


Figure 5.4: Set-up for the test of accuracy.

interference signal is of the form

$$I(t) = a_0 + a_1 \cos(2\pi f_1 t + \phi_1) + a_2 \cos(2\pi f_2 t + \phi_2), \quad (5.3)$$

where $\phi_1 = 4\pi L/\lambda_1$ and $\phi_2 = 4\pi L/\lambda_2$ are the interferometric phases at each wavelength. By feeding this signal to both probe inputs of the superheterodyne module, one gets

$$I_{\text{dem}}(t) = a_{12} \cos[2\pi(f_1 - f_2)t + (\phi_1 - \phi_2)]. \quad (5.4)$$

This signal has a frequency $f = f_1 - f_2$ and a phase $\phi = \phi_1 - \phi_2 = 4\pi L/\Lambda$ which is only sensitive to the synthetic wavelength Λ .

Stabilization of the two Nd:YAG laser sources

A synthetic wavelength of 200 mm corresponds to a frequency difference of 1.5 GHz. In order to demonstrate $2\pi/1000$ phase accuracy, this difference had to be stabilised with a relative accuracy better than 10^{-3} . To achieve this, the beat frequency resulting from the superposition of the two laser beams was measured by means of a high-speed photodetector (Newport amplified detector) and a frequency counter (HP53131). The beat frequency was measured with an integration time of 100 ms at a rate of 2 Hz and the feedback loop was implemented in software using LabVIEW. Figure 5.5 shows the

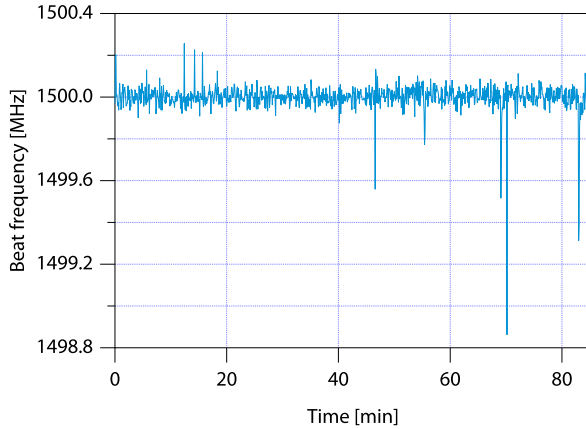


Figure 5.5: Stabilisation of the beat frequency between the two lasers.

remaining fluctuations of the beat frequency with the stabilisation loop. The standard deviation was measured to be 70 kHz, corresponding to a relative stability of 5×10^{-5} .

Results of the test of accuracy

The translation stage was moved in steps of 0.9 mm over 90 mm, and the phase was measured with the phasemeter prototype. The measurements were averaged over 4 samples, leading to a detection bandwidth of 50 kHz.

A straight line of slope $4\pi/n\Lambda$, where n is the index of refraction (estimated to about 1.0003), was fitted to the results and the deviations of the measurements were calculated. Figure 5.6 shows the results of these measurements. One can see that the deviations do not exceed ± 4 digits. The standard deviation was calculated to be 2.4 digits, corresponding to a standard deviation of the phase of $2\pi/850$ (the averaged output of the phasemeter prototype was on 2048 bits,) which is better than the target resolution of $2\pi/660$.

5.1.3 Dynamic tests

The movement of the delay lines introduce a Doppler shift in the heterodyne frequencies. If the phase responses of the 450 and 650 kHz filters have different shapes, an unwanted

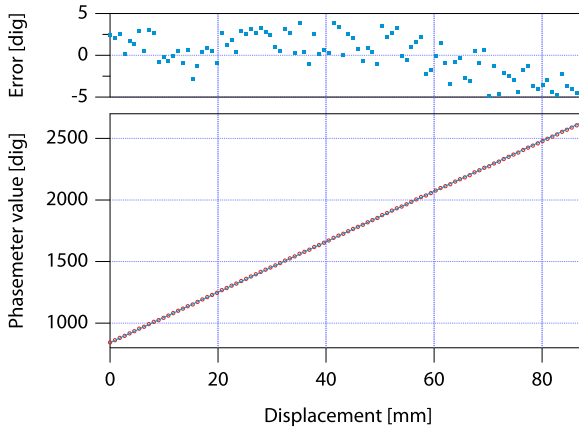


Figure 5.6: Results of the test of accuracy.

phase shift dependent on the velocity of the delay lines will be introduced between the reference and the science channels. The purpose of the dynamic tests was to verify that this phase shift was below the required accuracy of $2\pi/130$.

A loud speaker was used to achieve the velocities in the range of ± 12 mm/s corresponding to the movement of the delay lines. The measurements were performed in two steps, first the simulation of the movement of the differential delay line and the characterisation of the movement of the loud speaker and then the simulation of the movement of the main delay lines.

Simulation of the movement of the differential delay line

Figure 5.7 shows the optical set-up used to simulate the movement of the differential delay line. The 650 kHz signal for the probe channel was taken from the reference interferometer so the phase of the superheterodyne signal was dependent on the movement of the loud speaker.

Figure 5.8 shows the measured position of the loud speaker and the corresponding velocity obtained by its first derivative. The speaker was driven by a $1.5 V_{pp}$ signal at 1 Hz, reaching velocities of ± 15 mm/s. The sampling rate was 10 kHz.

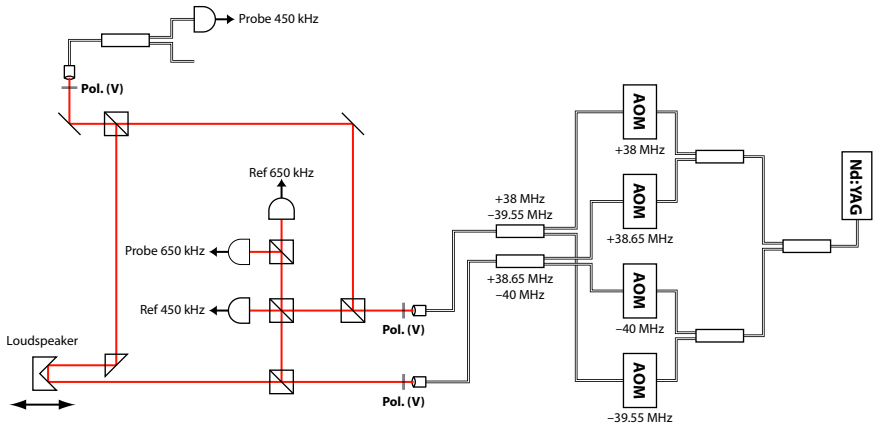


Figure 5.7: Optical set-up for the simulation of the movement of the differential delay line.

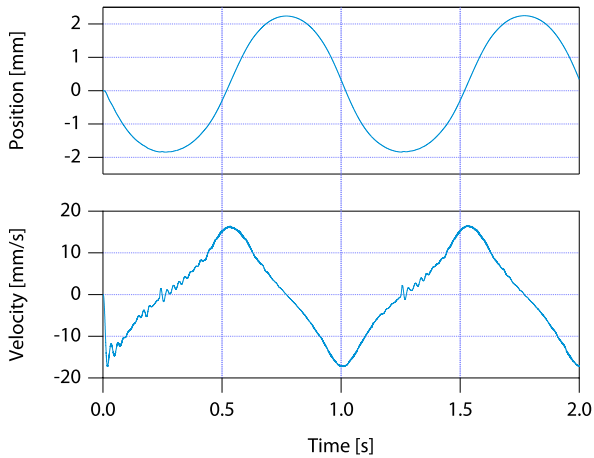


Figure 5.8: Measured position v.s time of the loud speaker and the corresponding velocity to simulate the movement of the differential delay line.

These measurements also show that the phasemeter was not skipping any fringes when the loud speaker was moving at velocities between ± 15 mm/s. Indeed, the skipping of a fringe would introduce a jump of half a wavelength between two successive samples. Since the measurements were taken at a frequency of 10 kHz, such a jump would give rise to a spike in the velocity profile of 6.6 mm/s. It can be seen from Fig. 5.8 that there are no such spikes.

Simulation of the movement of the delay lines

Figure 5.9 shows the set-up used for the simulation of the movement of the delay lines. The signal applied to the loud speaker was the same sine signal as in the differential delay line phase. Figure 5.10 shows the movement of the loud speaker (measured during the previous phase), the deduced velocity and the measured phase shifts introduced by the movement of the loud speaker, for velocities between ± 12 mm/s.

The phase difference ϕ_{corr} caused by the 78 MHz frequency offset between both heterodyne interferometers was calculated from the movement of the loud speaker and subtracted from the measured values in common mode:

$$\phi_{\text{corr}}(t) = \frac{\Delta v}{v} \frac{4\pi v}{c} L_{\text{LS}}(t), \tag{5.5}$$

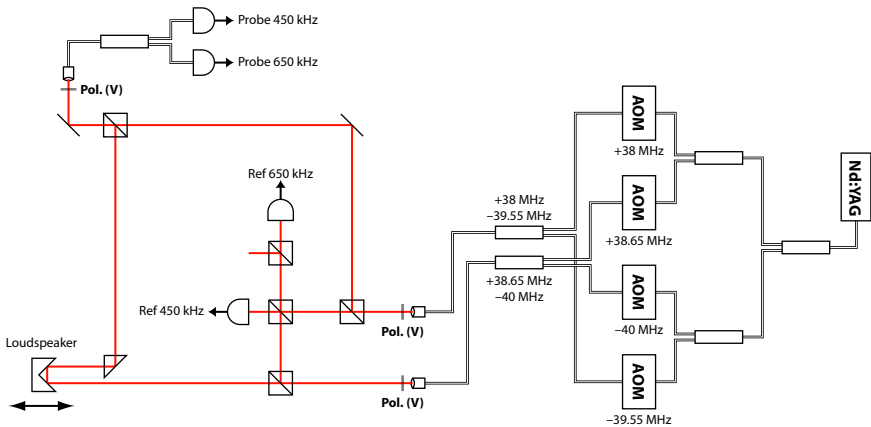


Figure 5.9: Optical set-up for the simulation of the movement of the delay lines.

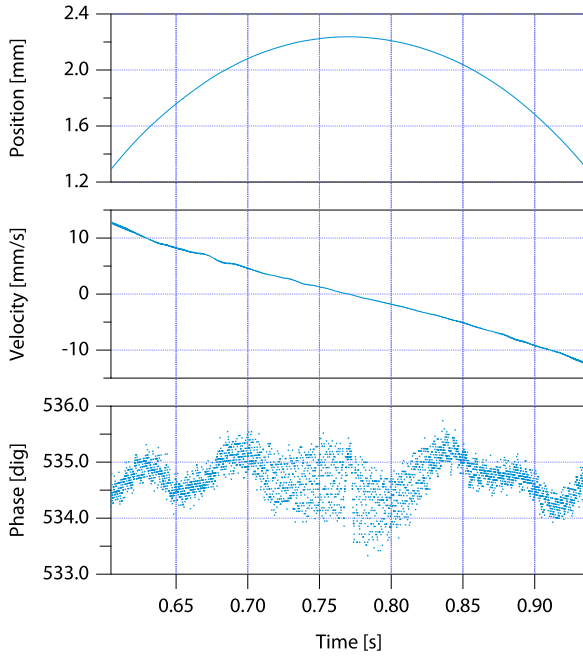


Figure 5.10: Loud speaker position, velocity and corresponding phase shifts vs. time.

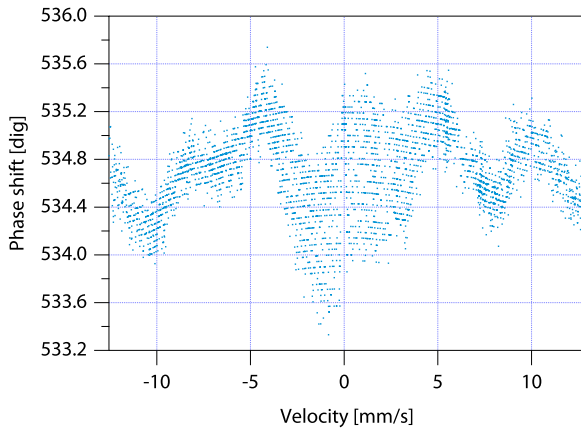


Figure 5.11: Phase shift vs. velocity.

where $\nu = 2.27 \times 10^{14}$ Hz is the the frequency of the laser, $\Delta\nu = 78$ MHz is the frequency offset between both channels and L_{LS} is the displacement of the loud speaker.

Figure 5.11 represents the corrected phase shifts as a function of the loud speaker velocities. The phase shifts due to the movement of the loud speaker do not exceed 2.4 digits, which corresponds to a phase accuracy of $2\pi/426$, which is much better than the required $2\pi/130$.

5.2 Tests of the laser stabilisation

5.2.1 Characterisation of the iodine cell

The absorption of the iodine cell was characterised at the Swiss Federal Office for Metrology and Accreditation (METAS) by means of a Burleigh 1500 wavemeter, in order to choose the absorption line to be used for the stabilisation and to determine its frequency.

In a first stage, the frequency of the laser (see chapter 4.4.5) was measured as a function of the voltage at the temperature tuning input. Figure 5.12 shows the result of a scan over the range of the temperature tuning input, between 0 and 8 V. One can see two mode hops of the laser within the working range, with a mode hop-free region between 227414 and 227430 GHz.

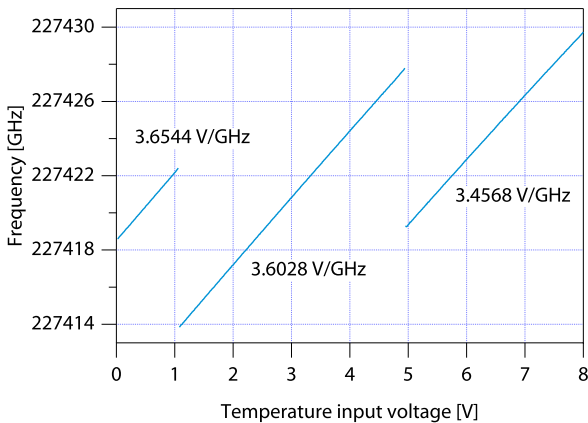


Figure 5.12: Characterisation of the temperature tuning input of the laser.

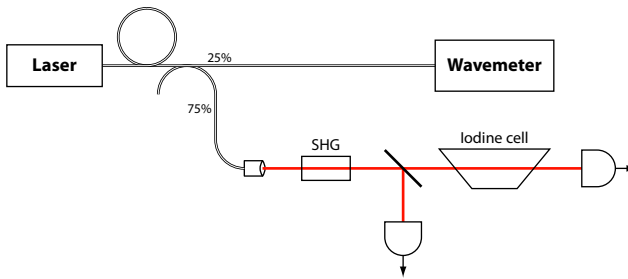


Figure 5.13: Set-up used for the characterisation of the iodine cell.

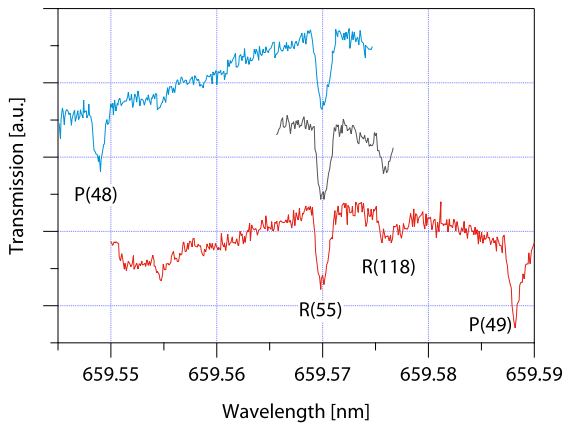


Figure 5.14: Transmission of the iodine cell.

Figure 5.13 shows the set-up used for the characterisation of the iodine cell. A 25/75 fibre coupler was used to split the laser beam in two arms, with 25 % of the light going into the wavemeter and 75 % in the LiNbO_3 SHG crystal. Two photodetectors were used in order to measure the optical power both at the input and output of the iodine cell, allowing for a normalised measurement of the transmittance of the iodine cell.

The results of these measurements are shown on Fig. 5.14. The three measurement sets correspond to the three mode-hop free regions of the laser. They have been superposed as a function of the wavelength. Four of the absorption lines of Table 4.2 can be identified,

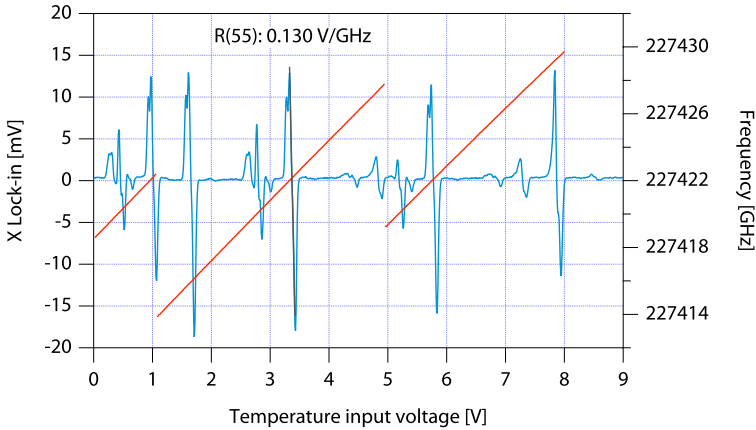


Figure 5.15: Temperature scan of the laser, with an absorption of the iodine cell of about 7 %.

the most promising one being R(55) as it is one of the strongest of the four and is conveniently located near the centre of the widest mode hop-free region of the laser.

As explained in chapter 4.4.3, the absorption of the iodine cell during these measurements was reduced to about 7 % due to the condensation of the iodine in the cold finger of the cell. However, the following measurements of the voltage sensitivity at the input of the photodetector were performed with the modified cell heating and the expected absorption of 25 %. Moreover, it was observed that at 25 MHz, the voltage sensitivity S_{VP} of the photodetector is only of $0.49 \text{ V}/\mu\text{W}$ instead of the expected $0.7 \text{ V}/\mu\text{W}$.

Figure 5.15 shows the first derivative of the transmission curve of the iodine cell over the range of the temperature tuning input of the laser (in blue), obtained by synchronously detecting the intensity at the output of the cell, as explained in chapter 4.2.3, along with the corresponding frequency of the laser (in red). The slope of the signal at the centre of each absorption lines was calculated, giving the voltage sensitivity S_{VF} . The value for the R(55) line is of $0.130 \text{ V}/\text{GHz}$. It is better than the minimum required voltage sensitivity at the output of the photodetector calculated in chapter 4.2.3, but lower than what could be expected from Eq. (4.12) in the current conditions.

Indeed, with an input power of $P_{in} = 12 \mu\text{W}$ and a voltage sensitivity of the photodetector of $S_{VP} = 0.49 \text{ V}/\mu\text{W}$, the expected voltage sensitivity at the output of the photodetector is of $S_{VF} = 0.412 \text{ V}/\text{GHz}$. However, it was shown by Nicolas Schuhler

and Samuel Lévêque at ESO that the absorption line is better approximated by a Gaussian function. In this case, the expected voltage sensitivity is of 0.266 V/GHz . The difference can be caused by a frequency excursion of less than 80 MHz in the EOM or by optical power losses between the SHG crystal and the detector.

5.2.2 Error signal monitoring

During the optimisation of the control loop, the easiest way to estimate whether the laser was properly stabilised was by monitoring the error signal. Indeed, if the voltage sensitivity at the output of the photodetector is known, the residual frequency fluctuations can be calculated from the value of the error signal and the voltage sensitivity measured with a temperature scan of the laser.

However, it must be noted that this is not a measurement of the absolute stability of the system. Indeed, any external factor that affects the error signal will be corrected by the control loop as if it were an error on the laser frequency.

Figure 5.16 shows the error signal for the laser in free running and in stabilised operation. Figure 5.17 shows the PSD of these measurements. One can see that the noise of the stabilised laser is below the required noise limit of $7.1 \times 10^4 \text{ Hz}/\sqrt{\text{Hz}}$ determined in chapter 4.1.3.

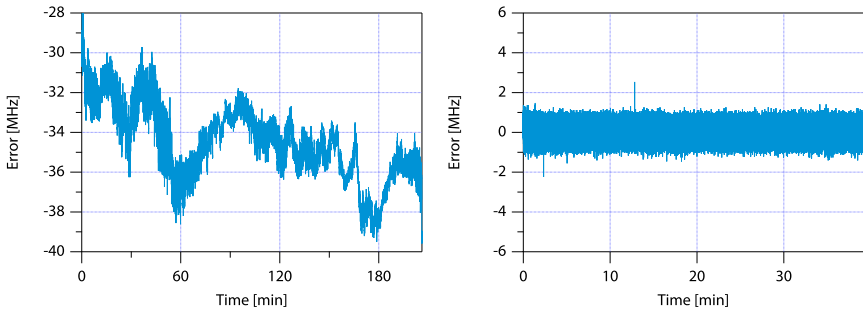


Figure 5.16: Error signal in free-running (left) during 206 minutes at a rate of 1 Hz and in stabilised mode (right) during 39 minutes at a rate of 1 kHz .

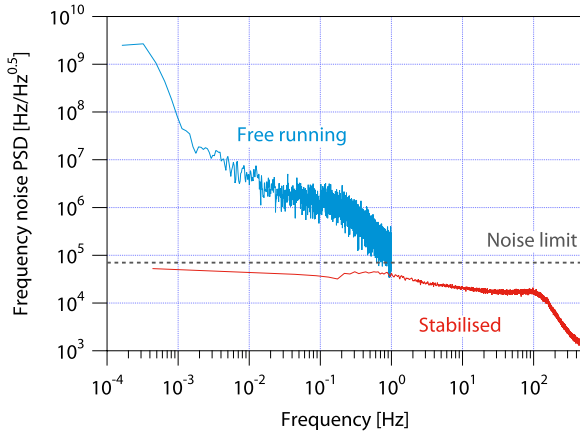


Figure 5.17: PSD of the error signal in free-running and in stabilised mode.

5.2.3 Test with long delay lines

The same test that was performed in chapter 4.1.2 to measure the frequency noise of the free running laser between 10 Hz and 10 kHz was applied to the stabilised laser. The frequency fluctuations of the laser were deduced from the phase fluctuations of an interferometer with a very large optical path difference achieved by a 1 km fibre delay. Figure 5.18 shows the set-up used.

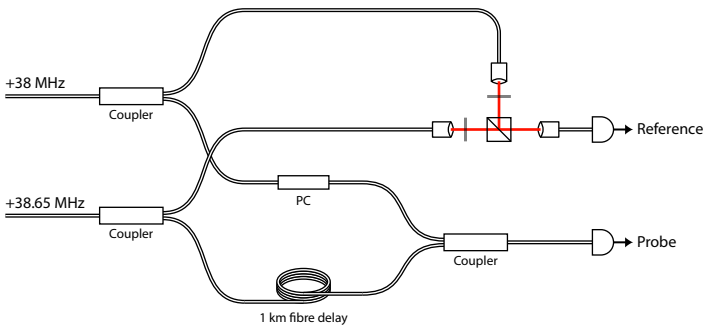


Figure 5.18: Set-up used for the test with long delay lines. PC: Polarisation controller.

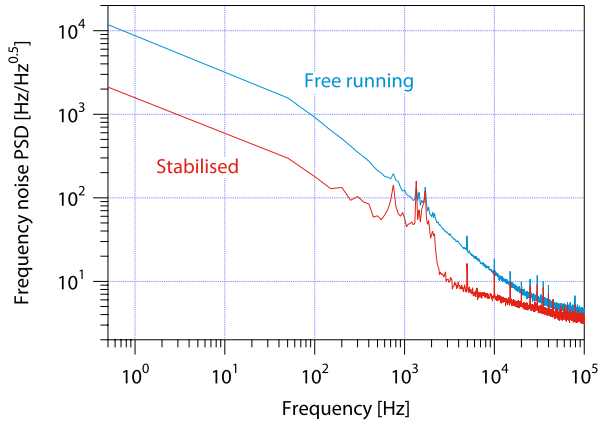


Figure 5.19: PSD of the frequency fluctuations of the free-running and stabilised laser.

Figure 5.19 shows the PSD of the frequency fluctuations of the free running and stabilised laser between 10 Hz and 10 kHz. One can see that they are both below the required noise limit of $7.1 \times 10^4 \text{ Hz}/\sqrt{\text{Hz}}$.

5.2.4 Further tests performed at ESO

After the stabilised laser was delivered to ESO, additional tests were performed by Nicolas Schuhler and Samuel Lévêque that showed slow fluctuations of the laser frequency that were outside the requirements. This section summarises the modifications that they made to the system in order to correct this problem, as well as the results of the tests performed to verify the performance of the improved stabilisation.

Redesign of the control loop

A new design for the control loop was introduced, in which two different PI controllers for the piezo and temperature inputs of the laser operate almost independently. In order to force the temperature loop to desaturate the piezo controller, the output of the piezo loop is added to the error signal at the input of the temperature loop, with a conversion factor that takes into account the tuning rate of the piezo input of the laser and the voltage sensitivity of the error signal.

Reduction of detection noise

As mentioned in chapter 5.2.2, any external factor that would affect the error signal (detection noise) would be interpreted as a variation of the laser frequency by the control loop. Three sources of detection noise were identified at ESO:

- electronic crosstalk at 25 MHz, originating from the cabling between the EOM and its driver;
- mechanical and acoustic vibrations affecting the 25/75 fibre coupler at the input of the system;
- residual amplitude modulation (RAM) at the output of the EOM.

The electronic crosstalk was reduced with a clean recabling of the EOM. The fibre coupler was removed and the dichroic filter is now used to collect the infrared light and reinject it into an single-mode, polarisation-maintaining fibre for the PRIMA metrology.

Part of the RAM could be reduced by adding a half-wave plate and a polariser at the input of the EOM to allow a better matching of the polarisation of the incoming beam with the axes of the EOM crystal. It was also determined that some RAM is introduced by a cavity effect in the crystal, whose length and refractive index change with the temperature [15]. Tests were made by regulating the temperature of the EOM, but no improvement was measured. Moreover, it was calculated that the temperature stability required to significantly reduce RAM due to the cavity effect is less than a tenth of a degree, which would add too much complexity to the system.

Tests with an optical frequency comb

The stabilised laser was brought to the Max Planck Institute for Quantum Optics (MPQ), Garching bei München who developed, through the firm MenloSystems, a self-referenced optical frequency comb generator [16], which provides extremely stable frequency references in a wavelength range between one and two micrometres. These tests of the frequency stability of the laser were performed with the help of Dr Ronald Holzwarth, from MPQ and MenloSystems.

A beat signal was generated between the frequency comb and the stabilised laser and was measured with a counter over 18 hours. Figure 5.20 shows the fluctuations of the beat

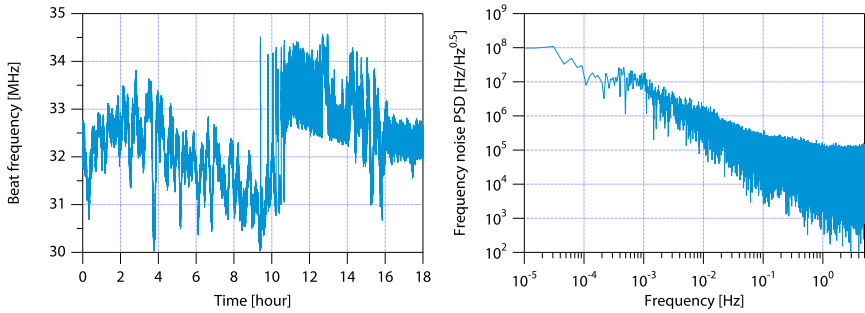


Figure 5.20: Fluctuations of the beat frequency between the frequency comb and the Nd:YAG laser (left) and PSD of the signal (right).

frequency and the PSD of the signal. The standard deviation is 808 kHz, which is below the specification of 2.2 MHz.

Chapter 6

Conclusion

Digital phasemeter for superheterodyne detection

A differential phase detection system for the PRIMA instrument of the Very Large Telescope Interferometer has been developed based on superheterodyne interferometry. The target accuracy was of 5 nm, with 1 nm resolution over a range of 100 mm and 20 nW of optical power. The heterodyne frequencies of 450 kHz and 650 kHz required to obtain a 200 kHz superheterodyne frequency were generated with four fibre-pigtailed acousto-optic modulators.

A superheterodyne detection module has been developed, that performs optical detection as well as electronic filtering and mixing of the heterodyne signals. The photodetectors have a sensitivity of $1.23 \text{ V}/\mu\text{W}$, a bandwidth of 7.7 MHz and a noise below -128 dBm/Hz . With a 55 kHz bandwidth and the minimum optical power of 20 nW, it corresponds to a signal-to-noise ratio of 55 dB, which is well over the required SNR of 40 dB. The input bandpass filters at 450 kHz and 650 kHz have a phase response that has been matched to 0.42° within the $\pm 55 \text{ kHz}$ bandwidth, resulting in a distance error of about 0.8 nm between the reference and science channels. This error is below the target resolution of the phasemeter. The SNR of the superheterodyne module was measured to be over 58 dB for electric signals equivalent to an optical power of 20 nW. The SNR was above the required 40 dB for equivalent optical powers as low as 0.2 nW.

A digital phasemeter based on Altera programmable logic devices has been designed. It uses a 200 MHz clock generated from the 200 kHz reference heterodyne signal by means

of a phase-locked loop, resulting in a $2\pi/1024$ phase resolution for a single measurement. It features a 19-bit integer fringe counter allowing for a range of 346 mm and can average phase data for arbitrary output rates between 0.5 Hz and 8 kHz. The rms resolution of the digital phasemeter was measured to be $2\pi/1678$ over 4000 samples, corresponding to a distance of 0.4 nm. The required resolution was $2\pi/660$. Tests of accuracy using two-wavelength interferometry on the phasemeter prototype showed an accuracy of $2\pi/850$. Dynamic tests reported a phase accuracy in common mode of $2\pi/426$ for delay line velocities between ± 12 mm/s, which is better than the required accuracy of $2\pi/130$.

Frequency stabilisation of a Nd:YAG laser

A set-up for the frequency stabilisation on iodine of a Nd:YAG laser at 1319 nm has been designed. The requirements are for a long-term frequency stability and calibration of 10^{-8} or 2.26 MHz. The second harmonic of the laser at 659.5 nm was generated by quasi-phase matching in a periodically-poled Lithium Niobate crystal. For an optical power of 50 mW in the fundamental beam focussed to $51.5 \mu\text{m}$ in the centre of the 20 mm long crystal, a second-harmonic power of $12 \mu\text{W}$ was obtained, corresponding to an efficiency of 2.4×10^{-4} .

Frequency modulation of the laser light, synchronous detection and a digital control loop are used to stabilise the laser frequency on the centre of an absorption line of iodine. The high frequency fluctuations are compensated by a Proportional-Integral regulator acting on the piezo input of the laser. A second PI regulator is used to desaturate the piezo actuator. Tests with an interferometer of large OPD (1 km fibre delay) showed that the frequency fluctuations between 10 Hz and 10 kHz are below the required noise limit of $7.1 \times 10^4 \text{ Hz}/\sqrt{\text{Hz}}$. Beat frequency measurements of the stabilised laser with a self-referenced optical frequency comb generator at the Max Planck Institute for Quantum Optics demonstrated a stability of 808 kHz over 18 hours.

Future work

Following the work presented in this thesis, a new project between the European Southern Observatory, Haute École Arc Ingénierie, and the Institute of Microtechnology has begun. It aims at improving the PRIMA laser metrology by means of an absolute metrology system based on multiple-wavelength interferometry [17].

Several lasers are stabilised on an optical frequency comb (FC1500, MenloSystems) provided by a mode-locked laser with appropriate frequency differences in order to generate the desired synthetic wavelengths. A new phasemeter for multiple-wavelength interferometry based on superheterodyne detection is also being developed.

Such an absolute metrology could reduce the complexity of the internal optical path calibration scheme of the VLTI and lead to an accurate determination of the baseline length, thus increasing the overall performance of PRIMA.

Acknowledgements

Now is the time to thank people, and I would therefore like to thank a number of people who know where their towel is [19].

First of all I would like to thank Professor René Dändliker for welcoming me in his group, giving me the opportunity of doing a PhD under his supervision, closely following my work and always being present when I needed his advice or support.

Yves Savadé who has been my supervisor throughout the project, for everything he taught me. I'm also especially grateful for his continuous availability even after he left the group.

Marcel Groccia, who designed and realised the analogue electronics and helped me a lot with the digital electronics as well as with my sadly necessary dealings in the underworld of Windows PCs.

Ali Pourzand who worked with me on the laser stabilisation. Working in the lab was much more fun when he was there, even when results were off by a factor of π^2 . Also, I need apologise for losing the Magic Hex Wrench, I'm afraid it was eaten by the Floor Kraken.

Samuel Lévêque who was responsible for my project at ESO.

Nicolas Schuhler

From ESO, Philippe Duhoux for his precious help on interfacing with the VLT operation software, Martin Dimmler for his advice on the design of the digital board, and also Frédéric Dérie, Françoise Delplancke, Andreas Glindemann and Reinhard Wilhelm for their involvement in the project.

From METAS, Rudolf Thalmann and Jacques Morel for their help with the characterisation of the laser.

From the Applied Optics Group, I would especially like to thank Iwan Märki, who defended his thesis the same week as I did, for his support in the home stretch, his friendship, all the serious, not so serious and downright not serious discussions we had, and also for taking to a beautiful local maximum of our country.

Olivier Ripoll, who was my assistant when I did my semester work, which gave me the opportunity to appreciate the good atmosphere in the lab.

The people I shared an office with: Piero Tortora, Yves Salvadé and Sylvain Jaquet.

Bibliography

- [1] F. Delplancke, S. A. Lévêque, P. Kervella, A. Glindemann and L. D’Arcio, “Phase-referenced imaging and micro-arcsecond astrometry with the VLTI,” in P. J. Lena and A. Quirrenbach, eds., “Interferometry in Optical Astronomy,” vol. 4006, pp. 365–376, SPIE (2000).
- [2] S. A. Lévêque, R. Wilhelm, Y. Salvadé, O. Scherler and R. Dändliker, “Toward nanometer accuracy laser metrology for phase-referenced interferometry with the VLTI,” in W. A. Traub, ed., “Interferometry for Optical Astronomy II,” vol. 4838, pp. 983–994, SPIE (2003).
- [3] R. Dändliker, R. Thalmann and D. Prongué, “Two-wavelength laser interferometry using superheterodyne detection,” *Opt. Lett.* **13** (5), 339–341 (1988).
- [4] Y. Salvadé and R. Dändliker, “Limitations of interferometry due to the flicker noise of laser diodes,” *J. Opt. Soc. Amer. A* **17** (5), 927–932 (2000).
- [5] T. Dennis, E. A. Curtis, C. W. Oates, L. Hollberg and S. L. Gilbert, “Wavelength references for 1300-nm wavelength-division multiplexing,” *J. Lightwave Technol.* **20** (5), 776–782 (2002).
- [6] A. Arie, M. L. Bortz, M. M. Fejer and R. L. Byer, “Iodine spectroscopy and absolute frequency stabilization with the second-harmonic of the 1319-nm Nd:YAG laser,” *Opt. Lett.* **18** (20), 1757–1759 (1993).
- [7] R. V. Pound, “Electronic frequency stabilization of microwave oscillators,” *Rev. Sci. Inst.* **17** (11), 490–505 (1946).

- [8] R. W. P. Drever, J. L. Hall, F. V. Kowalski, J. Hough, G. M. Ford, A. J. Munley and H. Ward, "Laser phase and frequency stabilization using an optical-resonator," *Appl. Phys. B* **31** (2), 97–105 (1983).
- [9] A. Yariv and P. Yeh, *Optical Waves in Crystals*, John Wiley & Sons, Inc. (1984).
- [10] A. Yariv, *Optical Electronics*, CBS College Publishing, 3rd ed. (1985).
- [11] A. K. Ghatak and K. Thyagarajan, *Optical Electronics*, Cambridge University Press (1989).
- [12] B. Boulanger, J. P. Feve and Y. Guillian, "Thermo-optical effect and saturation of nonlinear absorption induced by gray tracking in a 532-nm-pumped KTP optical parametric oscillator," *Opt. Lett.* **25** (7), 484–486 (2000).
- [13] F. C. Zumsteg, J. D. Bierlein and T. E. Gier, "K_xRb_{1-x}TiOPO₄: A new nonlinear optical material," *J. Appl. Phys.* **47** (11), 4980–4985 (1976).
- [14] Y. Salvadé, *Distance Measurement by Multiple-Wavelength Interferometry*, Ph.D. thesis, Université de Neuchâtel (1999).
- [15] E. A. Whittaker, M. Gehrtz and G. C. Bjorklund, "Residual amplitude modulation in laser electro-optic phase modulation," *J. Opt. Soc. Amer. B* **2**, 1320 (1985).
- [16] D. J. Jones, S. A. Diddams, J. K. Ranka, A. Stentz, R. S. Windeler, J. L. Hall and S. T. Cundiff, "Carrier-envelope phase control of femtosecond mode-locked lasers and direct optical frequency synthesis," *Science* **288** (5466), 635–639 (2000).
- [17] Y. Salvadé, A. Courteville and R. Dändliker, "Absolute metrology for the Very Large Telescope Interferometer (VLTI)," in P. J. Lena and A. Quirrenbach, eds., "Interferometry in Optical Astronomy," vol. 4006, pp. 424–431, SPIE (2000).
- [18] S. Lévêque, Y. Salvadé, R. Dändliker and O. Scherler, "High-accuracy laser metrology enhances the VLTI," *Laser Focus World* **38** (4), 101–104 (2002).
- [19] *The Hitchhiker's Guide to the Galaxy*, Megadodo Publications, Light City, Ursa Minor Beta.